Florida International University
FIU Digital Commons

FIU Electronic Theses and Dissertations University Graduate School

3-28-2019

Nanoparticle-Based Spintronic Computer Logic Switch

Kevin Luongo
Florida International University, krl60@miami.edu

Follow this and additional works at: https://digitalcommons.fiu.edu/etd

Part of the Electrical and Electronics Commons

Recommended Citation

Luongo, Kevin, "Nanoparticle-Based Spintronic Computer Logic Switch" (2019). *FIU Electronic Theses and Dissertations*. 3962.
https://digitalcommons.fiu.edu/etd/3962

This work is brought to you for free and open access by the University Graduate School at FIU Digital Commons. It has been accepted for inclusion in FIU Electronic Theses and Dissertations by an authorized administrator of FIU Digital Commons. For more information, please contact dcc@fiu.edu.

FLORIDA INTERNATIONAL UNIVERSITY

Miami, Florida

NANOPARTICLE-BASED SPINTRONIC COMPUTER LOGIC SWITCH

A dissertation submitted in partial fulfillment of

the requirements for the degree of

DOCTOR OF PHILOSOPHY

in

ELECTRICAL AND COMPUTER ENGINEERING

by

Kevin Luongo

2019

To: Dean John L. Volakis
College of Engineering and Computing

This dissertation, written by Kevin Luongo, and entitled Nanoparticle-Based Spintronic Computer Logic Switch, having been approved in respect to style and intellectual content, is referred to you for judgment.

We have read this dissertation and recommend that it be approved.

____
Jean Andrian

____
Georgakopoulos Stavros

____
Pezhman Mardanpour

____
Sakhrat Khizroev, Major Professor

Date of Defense: March 28, 2019

The dissertation of Kevin Luongo is approved.

____
Dean John L. Volakis
College of Engineering and Computing

____
Andrés G. Gil
Vice President for Research and Economic Development
and Dean of the University Graduate School

Florida International University, 2019

© Copyright 2019 by Kevin Luongo

All rights reserved.

DEDICATION

This dissertation is dedicated to my family, friends, mentors and those who research in pursuit of scientific knowledge.

ACKNOWLEDGMENTS

I would like to acknowledge my advisor Dr. Sakhrat Khizroev and the NSF Center Energy for Efficient Electronics (E3S) for providing the guidance and environment necessary to explore and produce the work contained within this dissertation. I would like to acknowledge my committee members Dr. Irene Calizo, Dr. Jean Andrian and Dr. Pezhman Mardanpour for their support along the way. I would like to acknowledge my classmates/friends for all the motivational talks, including Mark Stone, Emmanuel Stimphil, Krystine Pimentel, Brayan Navarrete, Ping Wang, Jeongmin Hong, Ali Hadjikhani, and Rakesh Guduru.

ABSTRACT OF THE DISSERTATION

NANOPARTICLE-BASED SPINTRONIC COMPUTER LOGIC SWITCH

by

Kevin Luongo

Florida International University, 2019

Miami, Florida

Professor Sakhrat Khizroev, Major Professor

Spintronics is a rapidly growing research field due to scalability, integrablility within existing VLSI architecture, significantly reduced switching energy and latency while maintaining stable bit orientation (Spin-up, Spin-down). For the first time sub-5nm Spin Transfer Torque –Magnetic Tunneling Junctions (STT-MTJ) were investigated utilizing various Integrated Circuit (IC) fabrication techniques to evaluate novel concepts in logic switches.

Tunneling Magnetoresistance (TMR) was measured in STT-MTJ stacks of Ta/CoFeB/MgO/CoFeB/Ta with differing diameter ferrimagnetic CoFe2O4 nanoparticles (10nm, 4nm and 2nm) embedded in the MgO layer. MR was detected in the 2nm and 4nm particle devices and demonstrated evidence of single electron transport.

Tri-layer STT-MTJ devices were fabricated using a thin film stack of Ta/Ru/Ta/CoFeB(M1)/MgO/CoFeB(M2)/MgO/CoFeB(M3)/Ta. The overall diameter of the stack was reduced to sub-20nm using Focused Ion Beam (FIB) to mill away extra material. The coercivities of the ferrimagnetic CoFeB layers were modified during thin film deposition by altering sputter conditions. Field Applied- Magnetic Force Microscopy (FA-MFM) was used to detect four different magnetic intensities corresponding to three

discreet resistances in the singly addressed device, making this architecture a candidate for neuromorphic computational applications.

Lastly a lithographic-less architecture was developed to mass fabricate and electo-mechanically probe multi-layered, single point, sub-5nm particle based STT-MTJ devices using off-the-shelf anodized nanoporous alumina. Once fabricated, the devices were probed to measure their IV characteristics and magnetoresistance (MR). The unprecedented MR changes on the order of 50,000% at room temperature suggest quantum mechanical behavior.

TABLE OF CONTENTS

CHAPTER PAGE

1. INTRODUCTION ... 1
1.1. Motivation for Spintronics and Magnetic Tunnel Junctions (MTJ) Development ... 1
1.2. Unique Contribution of this Reported Spintronics Research ... 5

2. THEORETICAL BACKGROUND ... 9
2.1. Magnetics ... 9
2.2. Magnetic Material Classification ... 10
2.2.1. Diamagnetism 10
2.2.2. Paramagnetism 11
2.2.3. Ferromagnetism 15
2.2.4. Antiferromagnetism 19
2.2.5. Ferrimagnetism 20
2.3. Micromagnetism ... 20
2.3.1. Exchange Energy 21
2.3.2. Magnetostatic Interaction 22
2.3.3. Magnetocrystalline Anisotropy 23
2.3.4. Magnetostriction 24
2.3.5. Zeeman Energy 24

3. FABRICATION PROCESS ... 27
3.1. Introduction ... 27
3.2. Substrate Choice ... 29
3.3. Lithography ... 30
3.3.1. Photolithography 31
3.3.2. Electron-Beam Lithography 40
3.4. Thin Film Deposition ... 46
3.4.1. Physical Vapor Deposition 47
3.4.2. Chemical Vapor Deposition 50
3.4.3. Electroplating 51

4. EXPERIMENTAL RESULTS ... 53
4.1. Motivation and Introduction ... 53
4.2. Magnetic Tunnel Junction ... 54
4.3. Justification for sub-10nm STT-MTJ device fabrication ... 59
4.3.1. Atomic clustered quantum mechanical simulation 59
4.3.2. AFM experiment 60
4.3.3. FIB-MTJ 61
4.4. Current Contributions to State of the Art ... 62
4.4.1. Nanoparticle MTJ 62
4.4.2. Stacked 3D Structures and Results 68
4.4.3. Novel Approach to Mass Sub-10nm Device Fabrication 71

4.5. Summary 78

5. FUTURE WORKS 81

REFERENCES 84

VITA 93

LIST OF TABLES

TABLE PAGE

Table 1: AZ 5214 IR (Negative Tone IR) Recipe 39

Table 2: EBL Bilayer Lift-Off Process (Positive Tone) Recipe 45

Table 3: Pros and Cons of each device 79

LIST OF FIGURES

FIGURE PAGE

Figure 1-1: Trending transistor density per microprocessor 2

Figure 2-1: Diamagnetic illustration of inverse alignment to applied field...................... 10

Figure 2-2: Paramagnetic illustration of alignment to applied field 11

Figure 2-3: Plot of Langevin function [41] 12

Figure 2-4: Non linear M-H loop of ferromagnetic material 15

Figure 2-5: Plot illustrating spontaneous magnetization by the molecular field (magnetic stability is reached at point P) [42] 17

Figure 2-6: Anti parallel alignment of antiferromagnet with net positive magnetic moment 19

Figure 2-7: Anti parallel alignment of ferrimagnet with nonlinear net positive magnetic moment 20

Figure 2-8: Magnetic exchange based on grain shape 22

Figure 2-9: Magnetic hysteresis loops illustrating easy axis (left) and hard axis (right) 23

Figure 3-1: Lithographic process for fabricating multilayered device 28

Figure 3-2: Photolithographic process for patterning and etching oxide.......................... 32

Figure 3-3: Illustration of positive and negative photoresists... 37

Figure 3-4: Electron beam scattering patterns and effect on the resist 42

Figure 3-5: Two resist method demonstrating overhang for enhanced liftoff 44

Figure 4-1: Illustration of MTJ “ON” state, parallel (left) and “OFF” state, antiparallel (right) 55

Figure 4-2: Polarization levels in ferromagnetic layers corresponding to non-infinite and infinite TMR.. 56

Figure 4-3: Spin transfer torque forces acting on precession 58

Figure 4-4: Spin transfer torque effects due to direction of spin-oriented electron flow 58

Figure 4-5: Quantum mechanical simulations illustrating de-coherence above 10nm and coherence below 5nm vs time [94] 60

Figure 4-6: Illustration of MTJ stack on modified AFM tip (left), SEM of modified AFM tip (middle), switching current vs applied magnetic field (top right), and current vs resistance loop (bottom right) [95] 61

Figure 4-7: SEM of trimmed MTJ stack (top left), device rendering (bottom left), MR loop (middle), and experimental trending with theoretical switching current vs device size (right) 62

Figure 4-8: Cross section of pinned sub-5nm particles in magnetic tunnel junction stack 63

Figure 4-9: V-I curves for trace and retrace current directions. The characteristic Coulomb staircase steps are shown by thin arrows and marked by numbers 1 and 2 for trace and 4 and 5 for retrace. The STT switching currents are shown by thick arrows. The STT switching currents are marked as 3 and 6 for trace and retrace, respectively. (left) dV/dI-I curves for trace and retrace current directions (right) 64

Figure 4-10: Illustration of nanoparticle magnetization switching with respect to Fig. 4-9 V-I curve in chronological order 65

Figure 4-11: MR curve of nanoparticle-integrated STT-MTJ device at 0.05uA bias current 66

Figure 4-12: MR curve, 0.01uA bias current nanoparticle-integrate STT-MTJ device ... 66

Figure 4-13: m-H loops of stack (left), MFM images and corresponding switching states due to applied field (right) 69

Figure 4-14: I-V measurement data of the stacked 3D structure annotated with possible switching mechanism (left) and the three corresponding resistances (right) 70

Figure 4-15: SEM of 0.02µm aluminum oxide membrane anodic disk 71

Figure 4-16: Cross section of fabrication process in nanoporous alumina: a) nanoporous alumina, b) gold evaporation, c) copper electroplating, d) gold etch, e) MTJ stack deposition, and f) copper evaporation of common electrode (inset: blowup of final device in one nanopore) 73

Figure 4-17: SEM of anodic disk with copper electroplated wires 74

Figure 4-18: MFM size and space distribution of nanoparticles (left), TEM of MTJ stack with embedded nanoparticles (middle) and zoomed in TEM of single nanoparticle (right) 75

Figure 4-19: Resistance vs time with varied applied magnetic field using a 10nA current 76

Figure 5-1: Addressable MTJ array architecture 81

Figure 5-2: SEM images of photolithographed electrodes with 100nm Au lines between electrodes lithographed using EBL 82

Figure 5-3: SEM images of 100nm Au lines using EBL 82

LIST OF ACRONYMS

AFM	Antiferromagnet
AGM	Alternating Gradient Magnetometer
AMR	Anisotropicmagnetoresistance
AC	Alternating Current
CVD	Chemical Vapor Deposition
DC	Direct Current
DRAM	Dynamic Random Access Memory
EUV	Extreme Ultraviolet
FM	Ferromagnet
GMR	Giantmagnetoresistance
HMDS	Mexamethyldisilazane
MFM	Magnetic Force Microscopy
MR	Magnetoresistance
MTJ	Magnetic Tunnel Junction
MOKE	Magneto-Optical Kerr Effect
PMMA	Polymethylmethacrylate
PVD	Physical Vapor Deposition
RF	Radio Frequency
SRAM	Static Random Access Memory
STT	Spin Transfer Torque
TMR	Tunneling Magnetoresistance
UHV	Ultra High Vacuum
UV	Ultraviolet

1. INTRODUCTION

1.1. Motivation for Spintronics and Magnetic Tunnel Junctions (MTJ) Development

Today, one of the most promising and sought-after research fields in solid state physics is Spintronics and its integration into semiconductors [1]. The rapidly growing interest in this field is partially due to the limitations of traditional semiconductor fabrication which has been following Moore's law for almost five decades and due to the significantly reduced theoretical switching energy. Gordon E. Moore predicted the doubling of transistors in an integrated circuit roughly every 2 years[2]. His prediction proved accurate for several decades and eventually became known as Moore's Law in the semiconductor industry. A more accurate analysis describes the chip performance doubling every 18 months given the combined effect of both adding more transistors in a chip and increasing their performance[3]. This trend (Figure 1-1) using traditional fabrication and device theory is reaching its end due to the undesired quantum mechanical effects which occur on the scale size traditional devices are approaching. For example as the thickness of the dielectric decreases, quantum mechanical tunneling increases which causes gate leakage currents. In turn, the leakage disallows linear power scaling as the device scales causing the power density to grow[4]. Further as CMOS transistors scale down, their static power density (device off) and dynamic power density (device on) begin to converge. Thus, Moore's Law has reached saturation. Prolonging its growth has been a major focus of research in both universities and industry. It is noteworthy that at this -5-nm scale when the traditional CMOS technology fails because of undesired quantum-mechanical effects,

the same quantum-mechanical effects[5] becomes the bases for a new technology paradigm known as spintronics.

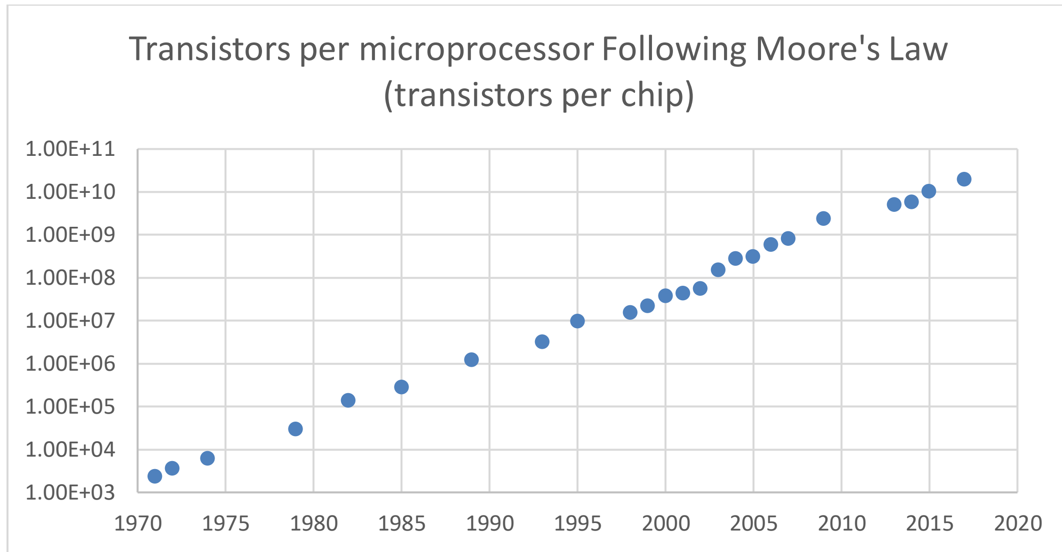

Figure 1-1: Trending transistor density per microprocessor

Spintronics makes use of the quantum mechanical spin degree of freedom of electrons for processing and storing information. Because of the wealth of new but poorly understood physics, it has evolved to be one of the most pursued research fields in solid state physics. The purpose of spintronics is to develop devices that exploit the electron spin degrees of freedom in addition to charge. One of the most prominent examples that helped propel the field of spintronics was the discovery of the giant magnetoresistance (GMR) effect in 1988[6], [7] and its application in modern hard disc drives. GMR effect is the significant difference of the electric resistance inherent to a layered stack of incorporated metallic magnetic layers separated by a non-magnetic spacer. GMR is dependent on the relative magnetized vector orientation of the ferromagnets[8]. The implementation of GMR has revolutionized the read head design of modern hard disc drives and thus has

enabled today's high-storage-density magnetic media[9]. For this reason, the discovery of GMR was honored by the awarding of the Nobel Prize in Physics in 2007 to Albert Fert and Peter Gru¨nberg and with the Millennium Technology Prize to Stuart Parkin in 2014.

Tunneling magnetoresistance (TMR) is a concept developed from GMR and led to the fabrication and implementation of the modern magnetic tunnel junction (MTJ). In the last decade, great efforts have gone into the development of non-volatile magnetoresistive random access memory (MRAM) with advanced capabilities of fast read and write, reduced power consumption, longer endurance, and integration in semiconductor electronic[10]–[12]. Due to this, the tunneling magnetoresistance (TMR) effect[13], [14] has drawn significant attention. TMR ratios have superseded GMR by an order of magnitude, with the highest recorded being ~600% [15] A magnetic tunneling junction (MTJ) has the same stacked layer as in case of a GMR device with the exception of a thin insulation layer, which replaces the non-magnetic metallic layer [13]. This structural change leads to a high sensitivity with a reduced energy consumption as it switches: lower current sensitivity for read-out of magnetization state and higher dependency of the resistivity on the relative orientation of the ferromagnetic layers for writing of information in the magnetization state, magnetic field pulses are applied in MTJ-MRAMs unlike the field assisted writing in the first generation of MRAMs. These magnetic field pulses are generated by the current flow through the microscopic wires close to the memory element. This technology has already lead to commercially available MRAM devices [16], [17]. But MTJ-MRAMs have the limitation of downsize scalability since writing currents are non-local and smaller memory elements will require higher switching fields [18].

With a recent MRAM innovation of the spin-transfer torque (STT) –MRAM, scalability has been improved [19]–[21]. In a STT-MRAM, magnetization is switched with the flow of spin angular momentum (or spin polarized currents) through the stacked layers. These spin polarized currents play a crucial role in writing and reading in new spintronics applications. This phenomena of "spin currents" has generated an alternative path to create and manipulate information [22]–[26] in ferromagnetic/non-magnetic metal bilayers for applications such as the spin pumping effect [27], [28] and the spin Hall Effect [29], [30]. However, with time STT-MRAMs suffer from degradation of the tunneling barrier. Since then a new form of magnetization switching has been developed which combines spin-transfer torques and spin-orbit torques [31], [32]. These combined effects do not need a flowing charge current through the MTJs, preventing the tunnel barrier degradation.

To understand these technological advancements it is important to have an insight of all the effects occurring at the ferromagnetic and non-magnetic material interface. However, multiple questions still remain unanswered with respect to a maximum efficiency of the spin transport across these interfaces, the ongoing physical processes, and the role of the non-magnetic materials used. For example, the non-magnetic material Pt, which is widely used in experiments concerning the spin Hall Effect and its inverse, has proven to be a very efficient material in the inverse spin Hall Effect due to its large spin-orbit coupling [27], [33], [34]. But a variety of values have been reported for the spin Hall angle, i.e., the efficiency to convert a charge current into a spin current, within the Pt layer [26], [35]. Due to these variations, other interfacial effects are being explored, such as an induced ferromagnetism at Pt interface [36]–[39]. Also, the role of a non-magnetic spacer layer in suppression of these interfacial effects is not understood.

1.2. **Unique Contribution of this Reported Spintronics Research**

Applying fundamental understanding of magnetism in classic and quantum physics (outlined in chapter 2) we characterized and utilized complex micro/nano-fabrication techniques (discussed in chapter 3) to demonstrate theoretical quantum-mechanical, magnetic spin behaviors in experimental quantum tunneling (STT-MTJ) devices built using novel sub-10 nm fabrication architecture (chapter 4) ultimately for the switching of computer logic bits. This work has for the first time proposed the following viable solutions to fundamental open questions of spintronics: (1) Demonstration of the feasibility of energy efficient magnetic memory and logic in devices in the sub-5-nm size range through using electric field assisted switching of magnetic states both for writing and reading information, (2) Demonstration of manipulation of spin states in such small devices through using quantum mechanical input and output instead of the traditional classical input and output, something which has never been done before and has the potential to pave the way to quantum computing.

Physics of spin devices in the sub-5nm range isn't well explored due to the difficulties in fabrication and characterization of devices in this dimension. Hence the focus here has been on the influence of the size of the memory and logic cells in the sub-5nm range and on the reliability of the new dynasty of computational devices. Also, when devices are driven by quantum mechanics in this size range, novel device concepts should be implemented. Traditional I-V characteristics of CMOS devices become obsolete in this size range. As a result, any observation of quantum properties in these devices is not taken advantage of and thus often considered as a drawback. On the other hand, it is widely accepted that the highly non-linear device properties owing to their quantum physics

promise superior characteristics compared to those by the traditional devices based on classical physics. However, to date, quantum mechanics based STT-MTJ devices do not exist in a consumer based electronic package such as a processor or as memory. We have hypothesized that if understood, this novel physical phenomenon could be favorably exploited to make memory and logic devices with extremely high data densities, above 100 TB/in^2, and data rates, above 10 TB/s. Particularly, we have shown that the traditional continuous crystalline quantum-mechanical models are not valid in this size range because the spin surface effects become significant and even start to dominate, compared to the volume effect, in the observed magnetotransport characteristics. Consequently, because of the significantly enhanced quantum-mechanical effects in this size range, e.g., the spin telegraph effect, the devices' inputs and outputs should also be considered in quantum-mechanical (not classical) terms. To build such small structures to address these fundamental questions, we have explored innovative fabrication and characterization approaches. One of the main ideas has been to use ultra-small magnetic nanoparticles embedded into magnetic junctions. Using nanoparticles presents a viable alternative fabrication approach not only for understanding the spin physics in this size range but also for mass production of future nanoelectronic/spintronic devices because of the availability of many well-established chemical processes to provide sub-5-nm nanoparticles with a very broad range of desired properties with an adequately high uniformity in size and composition. Sizes of the bits and duration of the switching pulses are selected to meet industrial requirements for a robust, low-cost memory or logic cell suitable to store small amounts of data. In an effort to understand the magnetization dynamics between adjacent non-magnetic and ferromagnetic layers in a stack, two ferromagnetic materials Ni81Fe19

(NiFe) and Co40Fe40B20 (CoFeB) have been investigated due to their general applicability in spintronic applications. Other commonly used materials in spintronics and their magnetization dynamics has been discussed. Several other nanoparticle based spintronics applications have been investigated.

The following chapters continue as such:

Chapter 2 gives an introduction to the theory of magnetics and magnetic properties. It presents the fundamentals of operation of magnetic devices. This is crucial to understanding the presented experimental work. In the beginning, concepts of magnetics are discussed followed by in-depth classification of the magnetic materials based on the magnetic properties. Discussion then moves to the various types of interfacial interactions in magnetic materials and their advantages over another. Understanding of these microscopic interactions is the key to realizing the impact of behavior of the devices discussed in this thesis.

Chapter 3 presents the micro and nano fabrication techniques for the sub-5nm spintronic devices in this work. Due to the fabrication challenges of such small devices, the underlying physics is still poorly understood. Each section initially summarizes the nano-fabrication method, materials involved in making of the device prototypes and later explain the specific parameters. Methods include: substrate preparation, photo/nano-lithography and thin-film depositions.

In chapter 4, all the results and discussions are presented categorically. Results of the numerical analysis for simulating the kinetics of spin excitations are given in section 4.1 along with references to theoretical spintronics to explain the numerical simulations results. Section 4.2 presents the switching mechanism of the prototype devices

and elaborates on their capability for multilevel logic in spintronics. Section 4.3 reviews prior contributions to state of the art while section 4.4 includes present contributions to state of the art and section 4.5 presents never before reported architecture the final prototype device of "porous alumina based nanoparticle spintronic computer logic switch". This architecture uses $CoFe_2O_4$, nanoparticles in a nanoporous structure. This mass fabrication of the "particle-MTJ" for creating logic devices for testing the novel spintronic hypotheses has experimentally demonstrated true quantum mechanical behavior with MR approaching unprecedented percentages at room temperature.

Chapter 5 summarizes the incomplete works and a future direction for the proposed prototype is also discussed.

2. THEORETICAL BACKGROUND

2.1. **Magnetics**

Materials can be classified according to how they respond to magnetic fields. When a field is applied, different materials experience different levels of flux inside compared to the outside. Materials with less flux compared to the outside, opposing the applied field, are diamagnetic. Materials with slightly more flux can either be paramagnetic or antiferromagnetic. Those that exhibit much greater flux are either ferromagnetic or ferrimagnetic. Additional measurements with varying temperatures provide more definitive information on the material classification. The magnetic flux density B is the amount of magnetic flux lines per unit area $\left(B = \frac{\Phi}{A}\right)$. Magnetic flux density can be expressed as the sum of the applied field (H) and the magnetization (M) where $B = H + 4\pi M$. Magnetization is the magnetic moment per unit volume $\left(M = \frac{m}{V}\right)$ and it is an intrinsic property of the material that depends on the collection and interaction of magnetic dipoles. The amount of magnetization depends on the applied field, and the rate at which a material is magnetized is called the susceptibility (χ). This dimensionless quantity represents how easily a material is magnetized in the presence of an applied field $\left(\chi = \frac{M}{H}\right)$. Diamagnetic materials have a small and negative susceptibility. Paramagnetic and antiferromagnetic materials have a small and positive susceptibility. Ferromagnets and ferrimagnets have very large and positive susceptibilities. The most common magnetic materials at room temperature are paramagnetic and diamagnetic, and are usually referred to as non-magnetic. In fact, the only room temperature ferromagnetic elements are Co, Fe, and Ni.

2.2. **Magnetic Material Classification**

In this thesis ferromagnetism will be discussed in much more detail than the rest, but some information on the other magnetic materials will be addressed. The atomic magnetic behavior will suffice to provide the reader enough detail to understand the distinction between magnetic materials:

2.2.1. **Diamagnetism**

These materials have a very weak interaction with external magnetic fields due to the non-cooperative behavior of the orbiting electrons. They do not have net magnetic moments, but when a field is applied a negative magnetization is produced, resulting in a negative susceptibility. Figure 2-1 illustrates diamagnetic behavior when influenced by external H-field. All materials exhibit a diamagnetic effect, but it is weak and overshadowed by paramagnetic and ferromagnetic effects. Typically, materials with filled orbital shells (no unpaired electrons) are net diamagnetic such as noble gases (Ar), many diatomic gases (H_2), some metals (Au), organic compounds, some ionic solids (NaCl), and materials with covalent bonds (Si). Susceptibility is in the order of 10^{-6} per unit volume.

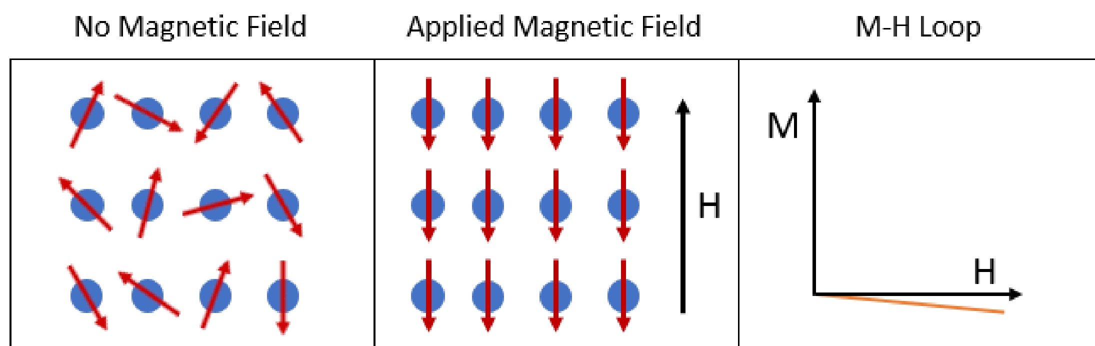

Figure 2-1: Diamagnetic illustration of inverse alignment to applied field

2.2.2. **Paramagnetism**

These materials exhibit a net magnetic moment due to unpaired electrons in partially filled orbitals as illustrated in Figure 2-2. Typical materials include some metals (Al), some diatomic gases (O_2), ions of transition and rare earth metals, salts, and oxides. The magnetic moments in these materials weakly interact with each other and are subject to random alignment due to thermal effects; therefore they have no net magnetization in the absence of an applied field. When a magnetic field is applied, these magnetic moments align in the direction of the field, resulting in a small yet positive susceptibility. Susceptibility is in the order of 10^{-3} to 10^{-5} per unit volume.

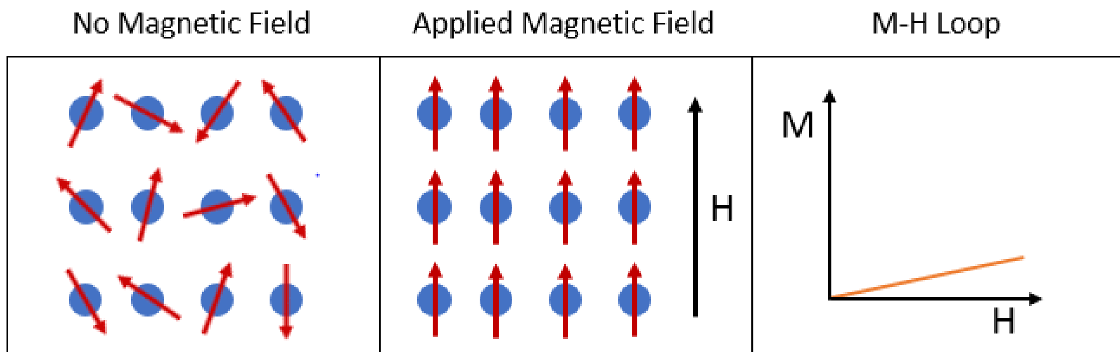

Figure 2-2: Paramagnetic illustration of alignment to applied field

Understanding paramagnetism leads to an understanding of ferromagnetism. There are several theories which differ according to the interaction of localized electrons. Langevin theory [40] describes paramagnetic materials by assuming that magnetic moments do not interact with each other and their random orientation due to thermal energy. Boltzman statistics can be used to describe the magnetic moment orientation with respect to the applied field:

$$e^{-E/k_BT} = e^{-m \cdot H/k_BT} = e^{-mH\cos\Theta/k_BT}$$

The number of magnetic moments between θ and $\theta+d\theta$ with respect to the field H is directly proportional to the fractional surface area of that's swept in a sphere. We can describe the probability as:

$$p(\theta) = \frac{e^{-mH\cos\theta/k_BT}\sin\theta d\theta}{\int_0^\pi e^{-mH\cos\theta/k_BT}\sin\theta d\theta}$$

Each moment contributes $m\cos\theta$ to the magnetization aligned to the field. The total magnetization:

$$M = Nm\frac{\int_0^\pi e^{-mH\cos\theta/k_BT}\cos\theta\sin\theta d\theta}{\int_0^\pi e^{-mH\cos\theta/k_BT}\sin\theta d\theta} = Nm\left[\coth\left(\frac{mH}{k_BT}\right) - \frac{k_BT}{mH}\right] = NmL(\alpha)$$

Where $\alpha = \frac{mH}{k_BT}$ and $L(\alpha) = \coth(\alpha) - \frac{1}{\alpha}$ which is the Langevin function (Figure 2-3). If we make α large be either increasing the applied magnetic field or decreasing the temperature, M becomes more aligned approaching Nm.

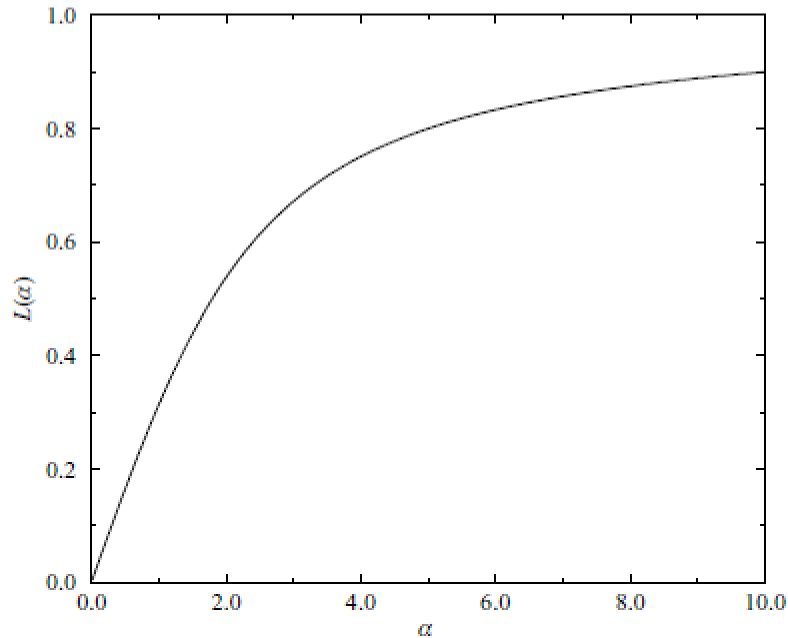

Figure 2-3: Plot of Langevin function [41]

The Langevin function can be expressed as a Taylor series[41], [42]:

$$L(\alpha) = \frac{\alpha}{3} - \frac{\alpha^3}{45} + \frac{2\alpha^5}{945} - \cdots$$

The first term dominates the series and the magnetization can be expressed as:

$$M = \frac{Nm\alpha}{3} = \frac{Nm^2H}{3k_BT}$$

This expression can give us the susceptibility and leads to Curie's law:

$$\chi = \frac{M}{H} = \frac{Nm^2}{3k_BT} = \frac{C}{T}$$

The Brillouin function includes quantization where magnetization is:

$$M = NgJ\mu_B\left[\frac{2J+1}{2J}\coth\left(\frac{2J+1}{2J}\alpha\right) - \frac{1}{2J}\coth\left(\frac{\alpha}{2J}\right)\right] = NgJ\mu_B B_J(\alpha)$$

The Brillouin function can also be expressed as a Taylor series:

$$B_J(\alpha) = \frac{(J+1)}{3J}\alpha - \frac{[(J+1)^2 + J^2](J+1)}{90J^3}\alpha^3 + \cdots$$

This expression also gives us the susceptibility and leads to Curie's law [41], [43], [44]:

$$\chi = \frac{J(J+1)Ng^2{\mu_B}^2}{3Tk_B} = \frac{C}{T}$$

Many paramagnetic materials don't necessarily follow Curie's law; instead they follow a more general expression called the Curie-Weiss law [41], [45]:

$$\chi = \frac{M}{H} = \frac{C}{T-\theta}$$

These materials exhibit some measure of spontaneous ordering and are ferromagnetic below a critical temperature known as the Curie temperature T_c [41]. Weiss operated under the assumption that there was an internal "molecular field" which described the interaction

between localized moments. This molecular field is proportional to the magnetization and material specific molecular field constant:

$H_W = \gamma M$

The total field acting on a paramagnetic material is:

$H_{tot} = H + H_W$

So, the susceptibility is:

$\chi = \frac{M}{H_{tot}} = \frac{M}{H+\gamma M} = \frac{C}{T}$, therefore $\chi = \frac{M}{H} = \frac{C}{T-C\gamma} = \frac{C}{T-\theta}$

Langevin theory assumes that electrons are localized to their atoms, and do not interact with other electrons outside of it. However, materials with good conductivity allow electrons to flow freely through the lattice, making this theory inapplicable for certain materials. Pauli paramagnetism utilizes the concept of energy bands to describe paramagnetism and is based on a collective effect of electrons [41].

In atoms electrons occupy discrete energy levels called atomic orbitals. When atoms are brought together the electronic configuration is altered and bands of allowable energy levels are formed. The greater the amount of overlap in the allowable energy levels, the greater the energy band. Electrons go occupying energy levels from the lowest energy state on up. The fermi level is the highest energy level that electrons fill when the temperature is 0K. Paramagnets have an equal amount of spin-up and spin-down electrons. However, when a magnetic field is applied, electrons whose moments align parallel with the magnetic field will have lower energy than those that are antiparallel. This creates a tendency for antiparallel aligned electrons to re-orient themselves with the applied field. Due to the Pauli Exclusion Principle, they would require enough energy to shift to an empty

parallel vacancy [41]. Only electrons close to the fermi level have the freedom to do so, since those that are buried deep don't have enough energy to promote itself to an empty slot. This difference in spin-up and spin-down orientations result in an overall magnetization. This susceptibility can be expressed as:

$$\chi = \frac{M}{H} = \frac{\mu_B^2 (N/V)}{E_F}$$

In this model the electrons are free and form a conduction band. Magnetization is due to the imbalance of spin-up and spin-down electrons, and is independent of temperature.

2.2.3. **Ferromagnetism**

Ferromagnetic materials, like paramagnets, have a net magnetic moment. Unlike paramagnets, these atomic moments exhibit very strong interactions due to quantum mechanical "exchange forces." Even in the absence of an applied magnetic field, these materials have spontaneous magnetization resulting in a non-zero net magnetization. There are only a few room temperature ferromagnets (Co, Fe, and Ni), but there are many alloys containing these elements that are ferromagnetic (CoFeB). Susceptibility in ferromagnets are 10,000-100,000 times greater (and more) than paramagnets.

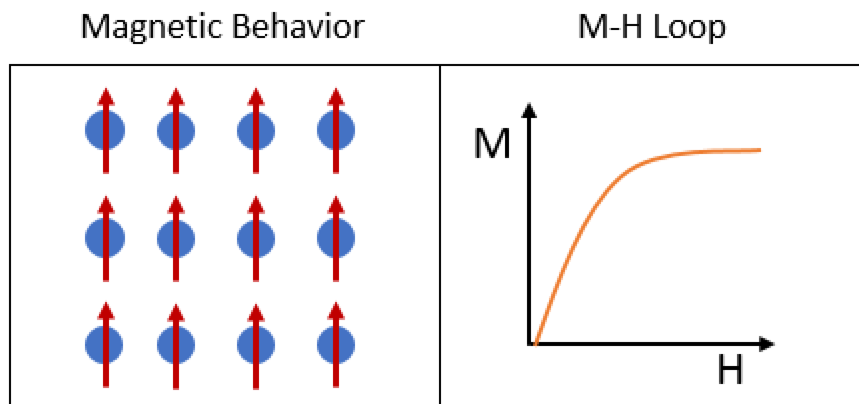

Figure 2-4: Non linear M-H loop of ferromagnetic material

Pierre Weiss was the first to make significant progress in understanding ferromagnetism [44]. Utilizing his ideas from molecular field theory (as described in paramagnetism subsection), he described ferromagnets as having large values of θ. He suggested that ferromagnets have strong molecular fields that magnetize a material to saturation as illustrated in Figure 2-4 even without the application of an external field. He also understood that ferromagnets are comprised of domains, which explain why we find ferromagnetic materials with a net magnetization of 0. An applied field effectively rotates the magnetic domains until they point into a singular direction, converting the material from a multidomain to a single domain.

Several theories describe ferromagnetism. Molecular field theory assumes localization of the magnetic moment to its corresponding ions. Magnetization is a function of both temperature and applied field, as though it were paramagnetic. However, assuming there is not an applied field, the only field acting on the specimen is the molecular field:

$$H_W = \gamma M$$

Weiss considered this field to be responsible for magnetizing the material. Temperatures above the Curie temperature would make a ferromagnet paramagnetic. Below this critical temperature it retains its spontaneous magnetization, and applying a magnetic field simply just rotates the magnetization in the direction parallel to the field. Plotting the molecular field line and superimposing it on the Langevin function; they intersect at 2 points, origin and a non-zero point (Figure 2-5). The point at the origin, however, is magnetically unstable and a small field, such as the Earth's field, is enough to increase its magnetization until it reaches the second point.

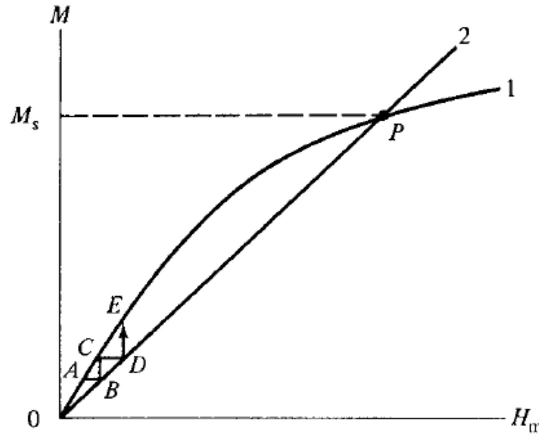

Figure 2-5: Plot illustrating spontaneous magnetization by the molecular field (magnetic stability is reached at point P) [42]

The point P on the graph above is magnetically stable and it corresponds to the point where the specimen is spontaneously magnetized. Weiss simply assumed that a ferromagnet is just a paramagnet with a huge molecular field. The origin of this field according to Heisenberg is due to exchange forces defined by quantum mechanics. This force is non-classical and depends on the orientation of the spins of electrons and is given by:

$$E_{ex} = -2J_{ex}S_iS_j$$

The exchange integral J_{ex} sign dictates the orientation between the spins. If it is negative, the spins align themselves in an anti-parallel orientation where the electrons can share the same orbit and will overlap spatially, resulting in stronger electrostatic repulsions. Ferromagnetism occurs when the exchange integral is positive and spins align themselves in a parallel orientation. These electrons occupy different orbitals due to the exclusion principle and also results in less electrostatic repulsion.

Weiss's molecular theory is valid for many cases except for those where electrons interact with each other, such as in metals. A free electron model describes good electrical conductors with more accuracy and is used to describe the only room temperature ferromagnets: Co, Fe, and Ni. They are first row transition metals where their outermost electrons are 3d and 4s. As these atoms come close to each other, their electron clouds overlap resulting in energy bands being formed. The fermi level for these 3 ferromagnets is located between the 3d and 4s bands. The density of states (DOS) is much greater in the d-band (holds 10 electrons) than in the s-band (holds 2 electrons). According to the rigid-band model, the valence electrons occupy both bands. The energy to promote a 4s electron to the 3d band and flip its spin orientation is not favorable compared to the exchange energy. In the 3d band there are many electrons near the fermi level, furthermore, this band is narrow with closely packed energy levels. This condition easily allows electrons to be promoted. Exchange forces prove favorable and a spontaneous magnetization occurs.

These materials with a strong enough applied field will result in magnetization saturation. If a small field is needed, they are categorized as magnetically soft. If a larger field is needed, they are magnetically hard. Past saturation, magnetic induction increases linearly with small gains, like a paramagnet. Furthermore, they exhibit hysteresis meaning that in the absence of a field or decreasing the applied field they still maintain their magnetization. Past saturation, when a magnetic field is removed, induction decreases from saturation B_S to retention B_R. The field required to bring the magnetization to zero is called the coercivity field (H_C), where low coercivities correspond to magnetically soft materials (~100 Oe) and high coercivities to magnetically hard ones (>5000 Oe). A typical BH loop starts from positive saturation field, goes to a negative saturation field, and back to a

positive one creating what is called a major hysteresis loop. Even if saturation isn't achieved, retention is still possible, creating a minor hysteresis loop. An infinite number of minor loops are possible but there can only be a single major one.

2.2.4. **Antiferromagnetism**

These materials are like ferromagnets in the sense that there are strong interactions between neighboring magnetic moments due to exchange forces. However, these forces promote an anti-parallel alignment of atomic magnetic moments rather than a parallel alignment, generating a net magnetization of zero. The absence of a non-zero spontaneous magnetization is why they are easily confused with paramagnets, but unlike them, they exhibit atomic magnet ordering (Figure 2-6). These materials remain antiferromagnetic below a critical temperature known as the Néel temperature (similar to Curie temperature). Above the Néel temperature they behave as paramagnets. The only element on the periodic table with room temperature antiferromagnetism is Cr. Many transition metals (Mn, Cr) and their compounds (MnO, Cr_2O_3) are antiferromagnetic.

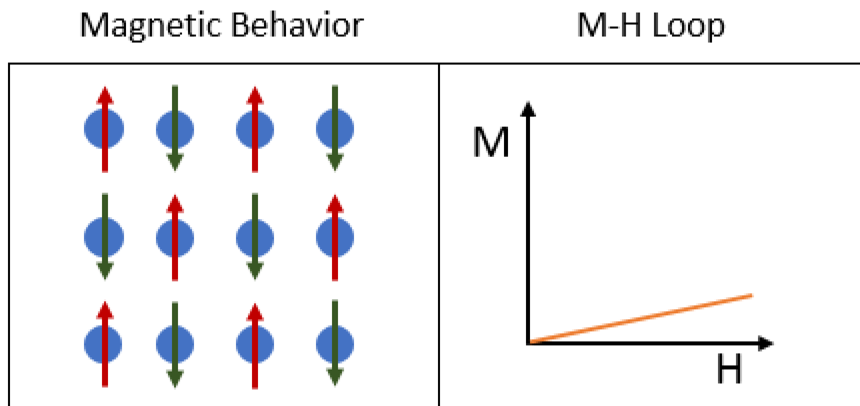

Figure 2-6: Anti parallel alignment of antiferromagnet with net positive magnetic moment

2.2.5. **Ferrimagnetism**

Ferrimagnetism is only observed on compounds and have very complex crystal structures. They have strong magnetic ordering, due to exchange forces, some leading to parallel alignment and others antiparallel. The net magnetization however is non-zero and breaks down into magnetic domains just like ferromagnetic materials, albeit with lower saturation magnetization as illustrated in Figure 2-7. Typical materials include magnetite, maghemite, and mixed oxides with iron and other compounds (cobalt ferrite).

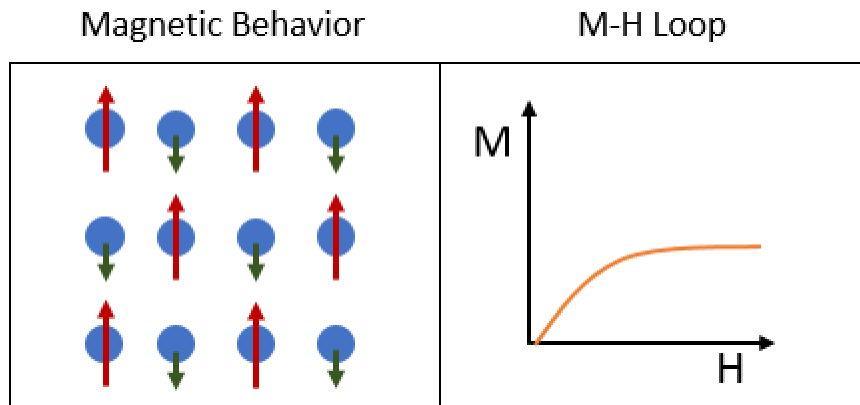

Figure 2-7: Anti parallel alignment of ferrimagnet with nonlinear net positive magnetic moment

2.3. **Micromagnetism**

There are many forces in magnetism that interact. These can be defined as energies competing with one another in a system. The main processes include: **exchange energy**, **anisotropy**, **magnetostatic interaction**, **magnetostriction**, and **Zeeman energy**. These interactions (and more) are important to understand since they impact the behavior of the devices fabricated in this dissertation. This section focuses on ferromagnetism at the microscopic level.

2.3.1. **Exchange Energy**

Exchange energy is responsible for ferromagnetism and consequently the spontaneous ordering of magnetic moments. This is a quantum mechanical effect where the wave functions of two identical particles are subject to exchange symmetry, where particles remain symmetric or antisymmetric when they exchange. As mentioned previously, this effect described by Heisenberg described the internal molecular fields in Weiss's theory [46]. The term "exchange" was used because when two atoms are brought together electrons from one atom is indistinguishable from electrons from a second and the possibility of them "exchanging" places is considered. This exchange energy, aside from ferromagnetism, is considered an important energy when dealing with molecules and the covalent bonds formed in solids.

For example, two atoms, atom i and atom j, are brought together and each have a spin angular momentum $S_i\hbar$ and $S_j\hbar$. Aside from electrostatic forces governed by Coulomb's law there is the exchange energy between both atoms that is defined as:

$E_{ex} = -2J_{ex}S_iS_j$ (same equation as in ferromagnetism subsection)

J_{ex} is the exchange integral which defines the intensity of the exchange coupling and the relative orientation of the spins [41]. The intensity of the exchange interaction also depends on the interatomic distances, decreasing with increasing atomic distances. We mentioned before that an antiparallel configuration occurs when the exchange integral is negative, minimizing the energy state (antiferromagnetism). When this exchange integral is positive, the energy state is minimal with a parallel configuration (ferromagnetism).

2.3.2. **Magnetostatic Interaction**

When a ferromagnetic specimen is composed of a single domain, it generates a field around it as illustrated in Figure 2-8. This field that surrounds the specimen acts in the opposite direction of the magnetization, hence it's known as a demagnetizing field. This demagnetizing field generates magnetostatic energy that is dependent on the shape of the specimen. To minimize this energy, the block is broken down into domains reducing the effect of the demagnetizing field. The magnetostatic energy can be brought to zero by arranging the domains in a way that eliminates magnetic poles at the surface. This, however, increases the exchange energy of the specimen because at the domain boundaries the magnetic moments are not parallel.

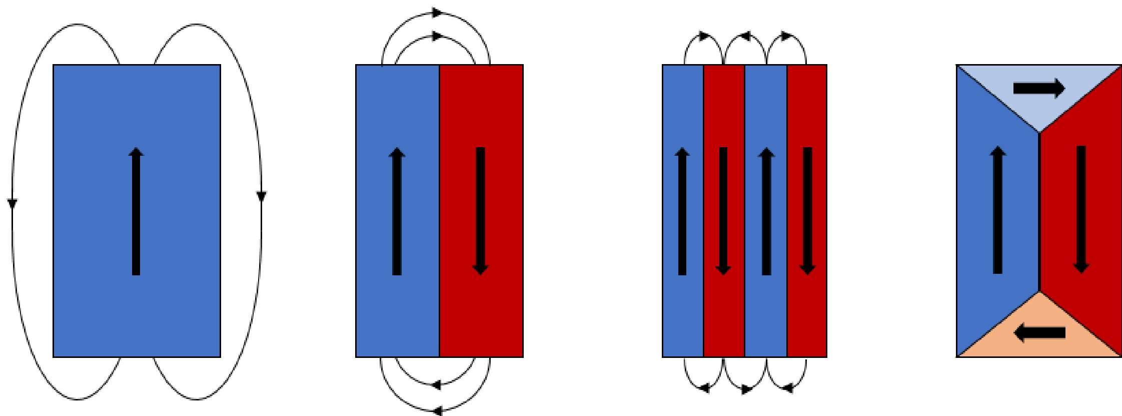

Figure 2-8: Magnetic exchange based on grain shape

The shape of the magnet plays an important role for creating preferential directions of magnetization and it is referred to as shape anisotropy. For example, if a sample is non-spherical, it will prefer to magnetize along its long axis rather than the short one. A perfect sphere will magnetize with an isotropic preference.

2.3.3. **Magnetocrystalline Anisotropy**

In addition to shape anisotropy there is also a dependence of the magnetization on the crystal structure. Magnetic properties change according to the crystallographic direction. There are preferred directions or “easy axis” where it is easier to magnetize a sample. Directions where it is harder to magnetize a sample are known as the “hard axis.” A larger field is needed to saturate a specimen along the hard axis than the easy one as illustrated in Figure 2-9. Magnetocrystalline anisotropy prefer large domains with few boundaries since the region between domains changes the direction of magnetization from an easy direction to a hard one.

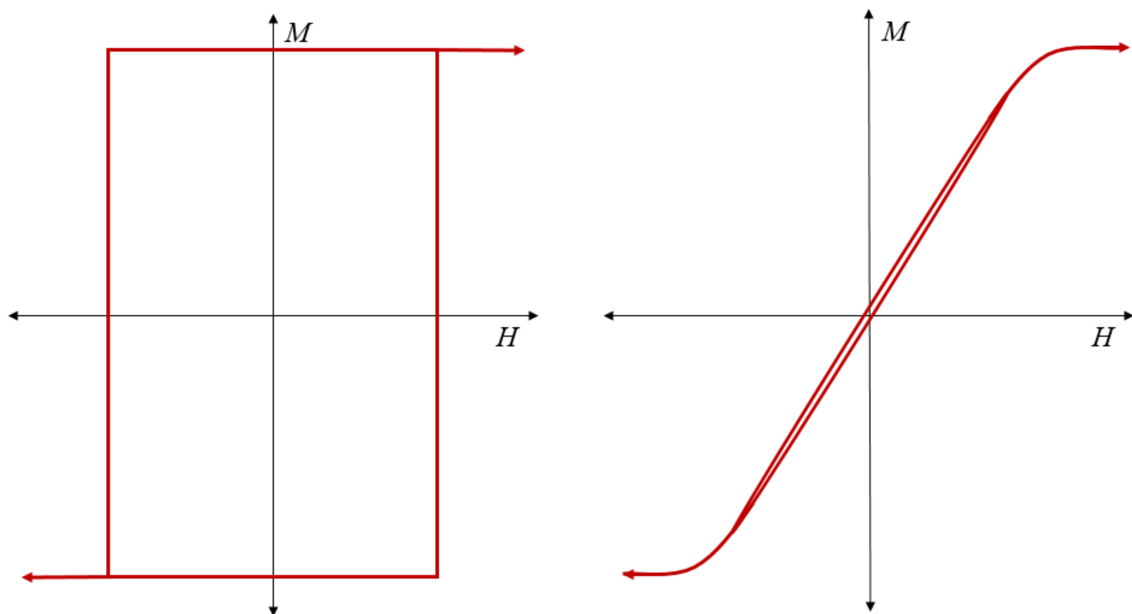

Figure 2-9: Magnetic hysteresis loops illustrating easy axis (left) and hard axis (right)

We can define the magnetocrystalline anisotropy energy as the energy difference per unit volume between the easy and hard axis. The energy needed to rotate a domain away from the easy axis is the energy required to overcome spin-orbit coupling. When changing the direction of the spin, the orbit follows suit. Any resistance is due to the strong

interaction between the orbit and the crystal lattice. Magnetic specimens with a single preferred direction (uniaxial anisotropy) [41], such as cobalt, can express the anisotropy energy as:

$$E = K_1 sin^2\theta + K_2 sin^4\theta + \cdots$$

The angle θ is between the magnetization vector and the easy axis. The K values are the anisotropy constants that vary from material to material and depend on temperature. Anisotropy energy decreases with increasing temperature. Above the Curie temperature, where a ferromagnet becomes paramagnetic, the anisotropy energy is zero [41].

2.3.4. **Magnetostriction**

When magnetizing a ferromagnetic specimen, it can undergo changes in length, a process called magnetostriction. Materials that elongate along the direction of magnetization are known to exhibit positive magnetostriction, while those that contract, contain negative magnetostriction. These changes in length are almost negligible, but they can alter the domain wall structure. An elastic energy term is added to the total energy and it is proportional to the volume of the closure domains. To minimize this energy there is a tendency to create smaller domains, which in turn creates additional domain wall. This, of course, increases both the exchange energy and magnetostatic energy.

2.3.5. **Zeeman Energy**

The Zeeman energy simply describes the interaction between the magnetization and an applied magnetic field. The energy can be expressed as follows:

$$E_Z = \int M \cdot H dV$$

It is essentially the energy required to rotate the magnetization by a certain angle with respect to the direction of the applied field. This value would be minimal when the magnetization and the external field are aligned in the same direction [45].

There are also methods to induce magnetic anisotropy to a material, an anisotropy that isn't intrinsic to the material. An example of one method is magnetic annealing that refers to heat treating a sample and letting it slowly cool in the presence of a magnetic field [44], [47]. This creates a directional order to the sample, allowing us to control the direction of preferred magnetization. Large magnetic anisotropy can also be created by a method called cold-rolling. For example, some samples can achieve magnetization parallel to the rolling direction via domain rotation. Irradiation can create defects which can also alter the directional ordering [48], [49]. There are many extrinsic methods that alter the anisotropy of a material (e.g., stress annealing, plastic deformation).

In addition to the prior classification of magnetic materials, there is another form of magnetism that is relevant: superparamagnetism. This occurs in small ferromagnetic and ferrimagnetic nanoparticles where magnetization can randomly flip direction due to thermal effects [50]. The time between magnetization flips is called the Néel relaxation time [51] and is expressed by the following equation:

$$t_N = t_0 e^{\left(\frac{KV}{k_B T}\right)}$$

Where t_N is the average time between magnetization flips, t_0 is a property of the material called the attempt time, K is the anisotropy energy, and V is the volume. When measuring the magnetization of the ferromagnet, if the time to flip magnetization takes longer than the Néel relaxation time, it will result in a net magnetization of zero. This

phenomenon is known as superparamagnetism and is similar to paramagnetism, except that the magnetic susceptibility is still much larger than paramagnet. As the particles become smaller, the energy barrier KV decreases resulting in an increased rate of switching. For volatile memory applications, the thermal stability ratio (KV/k_BT) must be greater than 20 [52]. This superparamagnetic effect limits the size of devices, which in turn limit the storage density of hard disk drives [41]. To overcome the thermal effect, ferromagnets with high anisotropy must be used for magnetic media. Unlike the coercivity field, which is an extrinsic field determined by crystalline imperfections, the anisotropy field is an intrinsic field mostly defined by the quantum-mechanical coupling between the spin and the orbit, known as L-S coupling. It is noteworthy that material science has significantly progressed and magnetic materials with an adequately high anisotropy field are easily available today, e.g., Co/Pd or Co/Pt multilayers or L_{10}-phase nanostructures. However, the increase of the anisotropy alone is not a solution. If the material has a coercivity field of above 2 T, as required for areal storage densities above 10 TB/in^2, the recording field generated by the write head must be higher than approximately 3 T. Because the recording field is limited to the saturation magnetization of the soft material of which it is made, that in turn is limited to approximately 2.6 T, according to the Slater Pauling curve [53]–[55]. Therefore, alternative approaches such as heat-assisted magnetic recording (HAMR) and microwave magnetic recording (MMR) have been proposed to use thermal and microwave energies, respectively, to assist recording into high anisotropy media with a magnetic field. However, both HAMR and MMR are not straightforward solutions owing to many technical difficulties to combine two different energy sources into one device.

3. FABRICATION PROCESS

3.1. Introduction

Despite all the theoretical energy advantages of spintronic devices in the sub-5-nm size range, the underlying physics is still poorly understood while viable device designs remain to be demonstrated. Arguably, the most difficult challenge in the pursuit to evaluate these open questions is the lack of robust nanofabrication processes to make such small scale devices for experimentation. This work aims to explore several nanofabrication techniques to build viable device prototypes that could be used for testing the theoretical limits helping pave the way to the paradigm of spintronics.

Microfabrication (and nanofabrication) is a collection of methods and technologies that facilitate the miniaturization process of making devices. These processes include lithography, etching, thin film deposition, etc. They are done sequentially, where the more fabrication steps involved increases the complexity, which is typically quantified as the mask count. Each mask represents a patterned step in the process and can range from just one single mask to as many as 30 or more.

Because a number of devices discussed in chapter 4 utilize the same general initial fabrication steps and because of the complexities involved in characterizing and understanding the nuances of each fabrication step, this chapter is dedicated to explaining the fundamentals in the methods involved in making the devices. All devices in the reported chapter utilize the same foundation of patterned and stacked thin films on an electrically isolated substrate which are addressed at the bottom and at the top of the stack via electrically conductive metal electrodes. An oxidized silicon wafer is used as a substrate represented by the color blue in figure 3-1. Step 1 photolithography using mask design 1

in conjunction with electron beam evaporation is used to pattern and deposit a titanium-gold thin film stack as a bottom electrode. Step 2 photolithography using a second mask design now in conjunction with sputtering is used to pattern and deposit the MTJ stack comprising of multiple thin films. Step 3 photolithography using a third mask and sputtering, patterns and deposits non-conductive alumina to prevent shorting between top and bottom electrodes. Finally step 4 is the same as step 1 but with a fourth mask to make the top electrode.   The specific fabrication steps and parameters will be referenced in the following chapters as will the details in additional fabrication processes.

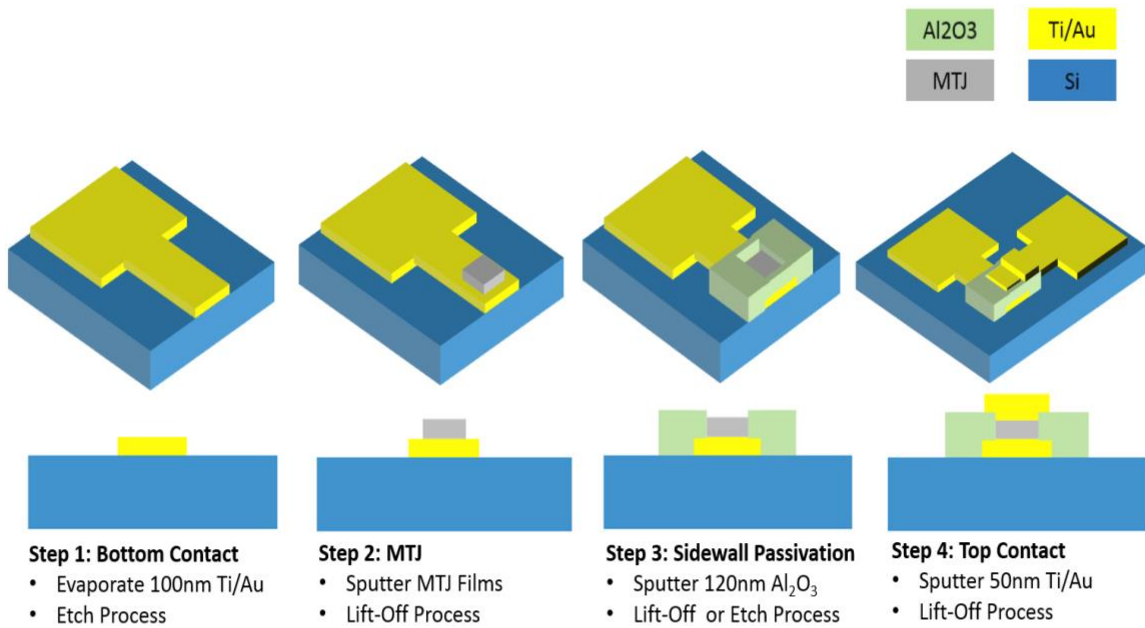

Figure 3-1: Lithographic process for fabricating multilayered device

3.2. **Substrate Choice**

The first step in any fabrication process is selecting an appropriate substrate since most micro- or nano- devices are not freestanding. The substrate can be an active part of your device or can simply work as a handle. Requisites in determining the right substrate include cost, ease of metallization, and machinability. In this thesis, silicon (Si) was chosen as the ideal substrate despite having a relatively high material cost. It is preferred due to its extreme flatness, mechanical robustness, and compatibility with many micromachining and film coating techniques. Its physical and chemical properties also make it a very versatile material choice for many microfabrication-based applications. Furthermore, most film deposition machines are designed to accommodate Si wafers making it also the most convenient to use. Historically, Si has been the substrate of choice for developing electronics and sensors.

Silicon substrates in this thesis serve only as a handle for the devices manufactured. More specifically, 4” prime silicon wafers, single-side polished with a 500um thickness were purchased. To ensure electrical insulation between the devices and the substrate, the silicon wafers were thermally oxidized, growing a conformal 300nm SiO_2 layer. Thermal oxidation is a standard process done in a furnace where an oxidizing agent diffuses into the silicon wafer and reacts with it at a high temperature (800-1200˚C) [56]. This is done in an inert environment to minimize the amount of impurities in the oxide.

Before and after the thermal oxidation process is done, the substrate is cleaned. Cleaning is necessary to remove any unwanted particles, grease, and free metal ions that can be destructive to the devices fabricated on the wafer. The cleaning process begins with a “solvent clean” and then followed by the standard RCA cleaning procedure,

except for the oxide strip. During the solvent clean process, the wafer is ultrasonicated in three separate baths; trichloroethylene bath, followed by an acetone bath, and then finally an isopropyl alcohol (IPA) bath [56]. The solvent clean is responsible for degreasing the wafer. RCA is a standard cleaning procedure developed specifically for silicon wafers and consists of two standard cleaning steps (SC-1 & SC-2) [56]. The first RCA step (SC-1) is a particle and organic clean where the substrate is cleaned in a solution that contains 5 parts deionized water (DI-water), 1 part 27% ammonium hydroxide, and 1 part 30% hydrogen peroxide. This step tends to leave a thin SiO_2 layer and some ionic contamination [57]. Typically, an oxide strip is done in aqueous 2% hydrofluoric acid, but this step is skipped after the thermal oxidization to prevent etching of the oxide grown. The next RCA step (SC-2), is an ionic clean where the substrate is placed in a solution made of 1 part 27% hydrochloric acid, 1 part 30% hydrogen peroxide, and 6 parts DI-water. This step removes the ionic contamination from SC-1. Finally, the wafer is rinsed in DI-water and dried with nitrogen. After cleaning, the wafers are able to undergo the microfabrication process.

3.3. **Lithography**

Lithography is one of the most important processes in microfabrication. It is responsible for patterning features onto the wafer and is followed by an additive (ex: film deposition) or subtractive process (ex: etching). The miniaturization process starts with lithography where a master pattern is transferred onto a wafer. It is mostly a top-down processing approach, where you start with a larger material, and you scale down to a smaller size. There are many different types of lithography (photolithography, x-ray lithography, charged-particle lithography, etc.), each offering certain advantages and

disadvantages such as pattern resolution, cost, throughput, time, etc. In this section, we will focus on photolithography and electron-beam lithography since they are the ones used in this thesis.

3.3.1. **Photolithography**

Photolithography is the most common form of lithography in microfabrication. It is a widely established and mature process since it is heavily used in industry, specifically in MEMS, sensor design, and IC fabrication. Known also as optical lithography and UV lithography, it uses light to transfer features from a mask to a light-sensitive polymer called photoresist [56]. Over the years, high resolution in photolithography has been achieved enabling the patterning of features as small as 0.1um. However, being able to resolve small features has come at the expense of the aspect ratio of the photoresist, limiting the process to very smooth surfaces and 2-dimensional features. Photolithography is done in a particle free environment called a cleanroom. A cleanroom is a special enclosed area that is also environmentally controlled (temperature, humidity, air pressure, vibration, and lighting). A cleanroom is classified based on the particle count and size per unit volume. The smaller the features to be fabricated, the smaller the acceptable particle size and particle count is allowed. Given the sensitivity of the photoresist to light, especially in the UV spectrum, photolithography is done in a "yellow" room, where the light fixtures are fitted with UV filters.

Before beginning the photolithographic process, a standard RCA clean is typically done. The following figure details the basic steps involved in photolithography with an etch process as illustrated in Figure 3-2:

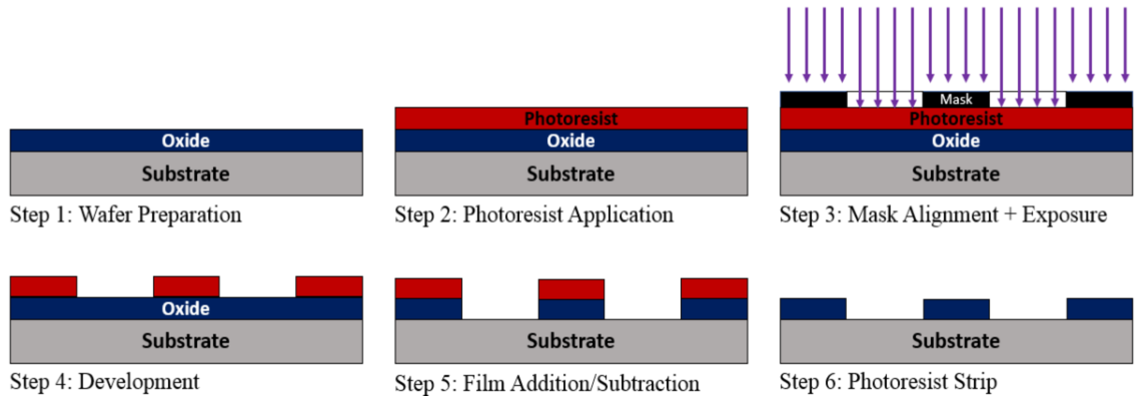

Figure 3-2: Photolithographic process for patterning and etching oxide

Step 1: Wafer Preparation

The first step is to heat the wafer at a high enough temperature to drive off any moisture on the surface and improve adhesion. Typically, this is done on a hotplate at 150°C for 8-10 minutes. This baking process is called the "pre-bake." To improve photoresist adhesion to the wafer (especially to oxides), hexamethyldisilazane (HMDS) can be spin coated beforehand [56]. Photoresist adhesion is a function of how hydrophobic the surface of the wafer is. Sputtering a sacrificial film can also be used as an alternative to priming the wafer with HMDS [58].

Step 2: Photoresist Application

After preparation, photoresist is then dispensed onto the wafer. Photoresist is a viscous, liquid solution that is applied onto a wafer that is spun at high speeds. This rapid spin ensures a uniformly thick coating across the wafer. The wafer can be spun anywhere from 1000 rpm to 5000 rpm. The faster the rotation speed of the wafer, the thinner the photoresist coating. This produces a layer as thin as a few hundred nanometers to hundreds of microns[59], [60]. The following formula is an empirical expression for calculating the expected thickness of the photoresist coated on the wafer:

$$T = \frac{KC^{\beta}\eta^{\gamma}}{\omega^{\alpha}}$$

Where **K** = calibration constant, **C** = polymer concentration, $\boldsymbol{\eta}$ = polymer intrinsic viscosity, **ω** = rotation of sample. The parameters **α**, **β,** and **γ** are exponential factors that need to be determined experimentally to predict the thickness of the polymer.

After spin coating, the wafer is baked to remove the liquid solvents in the photoresist and built-in stresses. This step is called the "soft-bake" and is typically done between 90-110°C for 30 to 90 seconds.

Step 3: Mask Alignment + Exposure

After the soft-bake, the wafer is ready for exposure. A mask is positioned above the wafer and is aligned by the user. The mask will only allow light to go through the transparent patterns, and block the areas which are opaque. A mask is a flat glass or quartz (transparent to UV) with patterned metal that is opaque to UV (ex: chromium). There are 2 methods of exposure: Contact and projection. In contact lithography, the mask makes physical contact with the wafer. This method is susceptible to defects in the pattern transfer and degrades the masks over time, but in R&D it is the most common method since it is much cheaper. Projection lithography uses high-resolution lenses to project the pattern from the mask onto the wafer. It can also reduce the mask pattern size by a factor of 5 or 10, facilitating the mask making process. This method, however, is very expensive and is mainly done in industrial settings.

Depending on the photoresist and thickness, different light exposure doses will be required (the time exposed under the light source). The dose is the product of the incident light intensity with the exposure time. For optimal pattern transfer, the light must

have the right directionality, intensity, spectral characteristics, and uniformity across the wafer. Photolithography uses light sources that can range from near ultraviolet (UV) to extreme ultraviolet (EUV).

After exposure, sometimes a "post-exposure" bake is done. This is done to reduce any standing wave phenomena due to the constructive and destructive interference patterns generated by the incident light from the exposure [61].

Step 4: Development

The exposed portion of photoresist changes the chemical properties of the polymer. There are two types of photoresist: positive and negative resists. Positive resists when exposed to light will become soluble while negative resists become insoluble. A solution, called the "developer," will remove the soluble portion of the photoresist, leaving behind the pattern transferred from the mask. Developers used to contain NaOH, but it has been found to be a major contaminant in MOSFET fabrication since sodium ions migrate into the gate oxide, degrading its performance [62]. This is important with regards to developing MTJs, since any metal ions can also deteriorate their performance. Metal-ion-free developers are preferred, such as tetramethylammonium hydroxide (TMAH). There are also dry development techniques, such as oxygen-RIE (reactive ion etching) [63]. They are used for higher resolution development.

A descum process is used to remove any unwanted residual resist remaining after development. This is usually done in an oxygen plasma asher. Residual resist is more common with thin resists of small features and high aspect ratios. This process will also thin the overall resist a bit. Sometimes a "hard-bake" is done after development to solidify the remaining photoresist. Residual solvents are evaporated and interface adhesion

between the resist and the wafer is improved. This step is usually done prior to an etching process, to improve hardness and the selectivity of the photoresist with respect to the etching agent.

Step 5: Film Addition/Subtraction

After developing an additive or subtractive process is used based on intended geometry. An etch process is performed, as shown in Figure 3-2 (Step 5), where the etching solution will only attack exposed regions of the wafer. Alternatively, we can add a thin film. Once a film is deposited, the resist is removed and only the exposed region will have the film remaining. Different photoresists and parameters facilitate either of these processes, but we will go into detail on that later. Any process done has to take into account any heat generated. You can run the risk of inadvertently baking the resist too much, making it difficult to strip off. For some photoresists, such as SU8, the polymer itself can become a permanent fixture on the wafer.

Step 6: Photoresist Strip

Once the photoresist is no longer needed, it needs to be stripped off from the wafer. A solvent or "photo stripper" is used so the photoresist no longer adheres to the wafer. Oxygen plasma can also be used in combination with a solvent. Dry stripping is becoming more popular since it is easier to control and stripping rates remain constant with time. Wet developing solutions tend to saturate after a certain point and are prone to accumulating contamination. Dry stripping also tends to be directional, making it preferable for achieving higher resolution. Since there are many different types of the resists, the manufacturer usually provides the best method to strip off the photoresist.

Photoresist can be classified according to its tone: positive and negative. When positive tone resist is exposed to light, the polymer weakens and becomes more soluble in developing solutions. Figure 3-3 illustrates the different results of positive and negative resists using the same mask. Positive resists are typically made from polymethylmethacrylate (PMMA) or a 2 component mix DQN made of photoactive diazoquinone ester (DQ) and a phenolic novolak resin (N). PMMA when exposed to EUV becomes soluble via chain scission. Chain scission is the breakdown of a polymer main chain caused by thermal stress or ionizing radiation [64]. DQN is sensitive in the near-UV spectrum. When exposed it photochemically transforms into a polar, base-soluble product. Positive resists are used more than negative resists when feature resolution is critical, having achieved sizes less than 0.5um. An overcut and vertical profile is typical of positive resists making them suitable for etch processes.

Negative tone resists when exposed to light strengthen the polymer bonds, becoming less soluble. The first resists used in semiconductor production were negative, and initially insolubility was achieved by a process called free-radical-initiated photo-cross-linking processes [65]. This insolubility is achieved either by increasing the molecular weight of the exposed resist or photochemically transforming it. Newer negative resists use the latter. Typically, a 2 component resist is used, containing bis(aryl)azide rubber resist with cyclized poly(cis-isoprene) as a matrix resin. A major drawback using this type of resist is its tendency to swell in developing solutions. This has limited the resolution to 2-3um. Since UV exposure is greater at the surface of the resist than at the interface, a natural undercut is typically formed making it ideal for a “lift-off” procedure.

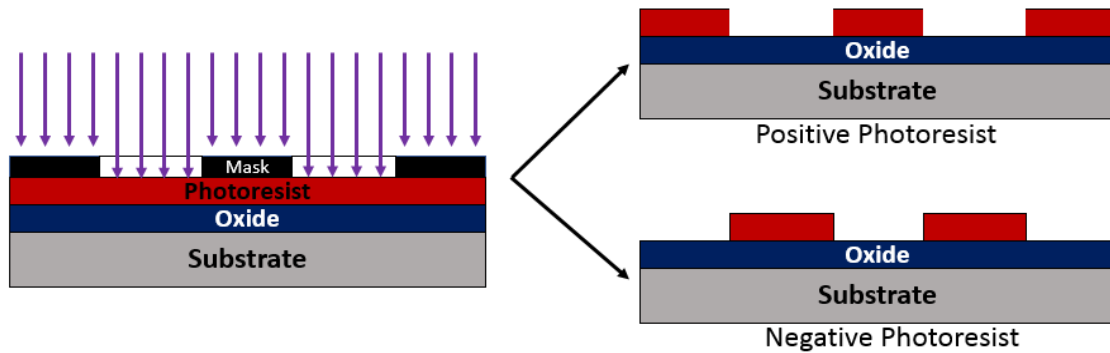

Figure 3-3: Illustration of positive and negative photoresists

Lift-off is mainly used in this research, and therefore an undercut profile is preferable. While negative resists are suitable for this, it is possible to create this profile with positive resists. A bi-layer process can be used, where the layer at the substrate-resist interface develops quicker than the layer on top, creating the desired undercut. An image reversal resist can also be used, a single layer process where the resolution of the positive is maintained but an undercut can still be created [66]–[68]. The exposed regions do become soluble (as would be expected from a positive resist), but then a reversal bake is done, where the exposed area become cross-linked while the rest remain photoactive. A flood exposure is done (no mask), causing the previously unexposed region to become soluble. This type of resist is also called “dual-tone” since it can act as both a positive and negative resist.

The “critical dimension” (CD) is the minimum feature size that can be consistently resolved in lithography [69]. Many factors govern the sustained resolution in a substrate, including mechanical stability of the hardware used, material properties, scattering of the light, etc. Critical dimension can be described with the following equation:

$$CD = k_1 \frac{\lambda}{NA}$$

The parameters $\mathbf{k_1}$ is an experimental coefficient that reflects process related factors, **NA** is the numerical aperture of the lens as seen by the substrate, and **λ** is the wavelength of the light source. While it may seem obvious that using a smaller wavelength will increase resolution, this also comes at the expense of the depth of focus. A change in depth of focus required us to address the thickness of the photoresist and the surface topology.

The type of photolithography done in this research used hard contact, where the mask is pressed against the substrate. While proximity alignment can also be done, higher resolution is achieved with direct contact. In addition to surface topography and unwanted particles, it is important to address the diffraction of the light. The intensity of the light is not necessarily uniform as it passes through the mask, particularly at the edge of an opaque figure on the mask. Diffraction can cause the edge to be blurred, affecting the resolution. For proximity printing, the following formula describes the minimum feature that can be resolved:

$$b_{min} = \frac{3}{2}\sqrt{\lambda\left(s + \frac{z}{2}\right)}$$

Where $\mathbf{b_{min}}$ is the minimum feature resolution, **λ** is the wavelength of light, **s** is the gap between the mask and the resist, and **z** is the thickness of the resist.

For contact printing, the gap s goes to 0, and the following formula applies:

$$b_{min} = \frac{3}{2}\sqrt{\left(\frac{\lambda z}{2}\right)}$$

It can be seen from the above equation that the resolution increases when we reduce the gap to zero. The problem with this method is the degradation of the mask over time.

The following recipe was characterized and used in this thesis for lift-off:

Table 1: AZ 5214 IR (Negative Tone IR) Recipe

Dehydration Bake	Hotplate 5min/120°C
Spin Coat	Resist Thickness: 1.2um Spin 1: 500 rpm Ramp 1: 250 rpm/s Time 1: 5 s Spin 2: 5000 rpm Ramp 2: 2500 rpm/s Time 2: 30 s
Soft Bake	Hotplate 1min/110°C
Exposure	60 mJ
Reversal Bake	Hotplate 1min/120°C
Flood Exposure (No Mask)	400 mJ
Development	300MIF Full Concentration, 40-50s
Descum	O_2 Plasma Etch for 60s

We mentioned earlier that decreasing the wavelength would improve the resolution of the resolved features. There are other illumination sources that can be used, such as EUV, x-rays, electron beams, etc. The following section we will describe electron-beam lithography, a method used extensively in this research.

3.3.2. **Electron-Beam Lithography**

Electron beam lithography (EBL) is a patterning technique that can achieve sub-10nm resolution. Patterns are written by scanning a focused beam of electrons across an electron-beam sensitive polymer [70]. The exposed polymer changes solubility, selectively removing or retaining it when immersed in a developing solution. The steps involved are similar to optical lithography with the exception that the pattern is directly written rather than transferred from a mask. As with optical lithography, it is also limited to 2 dimensional patterns. While it has the advantage of having much higher resolution, it has low throughput. Efforts are made to improve the volume output such as by adding parallel beams and projection EBL. In industry, they are limited to making high-resolution masks and direct writing on wafers for specialized applications. In a research lab, however, volume is not a major concern and it is an excellent tool to develop prototypes in the nanometer range. In this thesis, different types of devices were made using EBL.

An EBL system is essentially a scanning electron microscope (SEM) with the addition of a beam blanker and a pattern generator to control the areas to be exposed. A blanker is responsible for rapidly turning on and off the electron beam. Resolution is limited by the quality of the electron optics, resist, substrate, developer, and the process conditions. Quality optics are needed to generate a finely focused spot. Process conditions include selecting the appropriate beam energy and dose, carefully characterizing the development time and the temperature at which we bake the resist. Other issues include delocalization of electrons, line edge roughness, etc. Electron beam lithography is not straight forward, in order to achieve high quality, repeatable results the patterning process must be well characterized and carefully monitored step by step.

The first step to achieving high resolution EBL is to generate a stable, high brightness electron source. Electrons can be generated by heating a conducting material until the electrons have enough energy to overcome the work function barrier. Materials with low work functions, such as lanthanum hexaboride (~2.5eV), are preferred. Field electron emission sources use electrostatic fields instead of heat to generate electrons and are capable of generating a smaller beam spot. Photoemission can also be done by exciting electrons with enough energy from photons. Thermal field emission sources [71] are typically used though, since they tend to be more stable, which is important for long writing periods [72]. Electrons travel to the sample in a vacuum to minimize gas scattering. Depending on the energy and beam intensity, repulsion from electrons can also affect the beam size. Overall, a beam spot of a few nanometers can be achieved in most EBL systems.

When the electron is accelerated towards the resist, a series of low energy elastic collisions will occur, deflecting the electrons. As the electrons travel further down, this forward scattering effect is more pronounced. The beam is effectively broadened as it travels from the surface of the resist to the substrate/resist interface. This broadening effect is even more pronounced with low incident energies. The electrons can also penetrate the substrate and re-emerge at another point away from where they entered. These are called backscattered electrons (Figure 3-4), and they can cause exposure micrometers away from their point of incidence. These proximity effects can distort features, overexpose nearby patterns, or even create unintended exposures. While features as small as 10nm have been achieved, pitches have been limited to 20nm, due to proximity effects. Non-elastic collisions can also occur, generating low energy "secondary electrons" due to ionization. These tend to be short ranged but can also have an impact in the EBL

resolution. Electrostatic charging due to an insulating substrate will defocus the electron beam, requiring the use of a metal or conductive polymer above or below the resist to absorb the electrons [73].

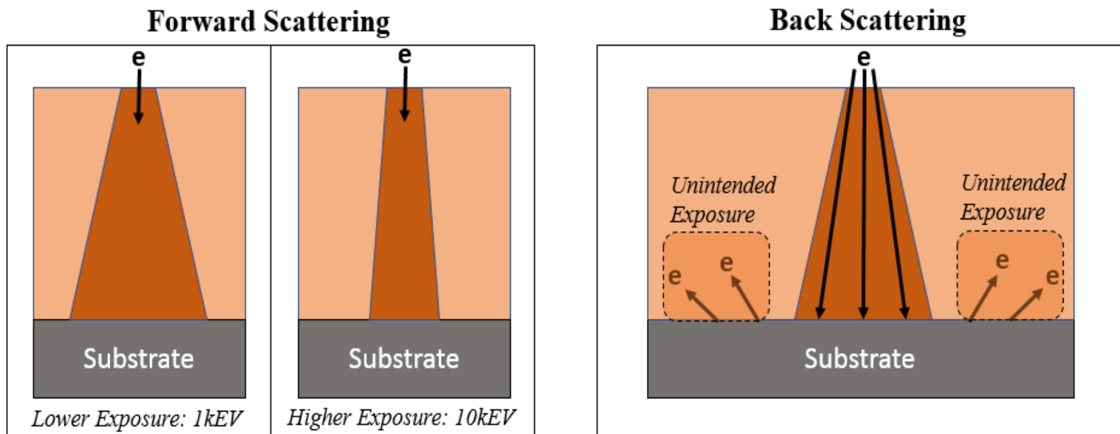

Figure 3-4: Electron beam scattering patterns and effect on the resist

Ideally, using higher voltages will reduce forward scattering, increasing the resolution. Aside from the trade-off with back-scattering effects, it also reduces the amount of inelastic collisions responsible for changing the solubility of the resist. For example, in PMMA, this results in less chain scissions per electron. Increasing the voltage clearly decreases the sensitivity, resulting in an increase in dose. Lower sensitivity is not desired since it is correlated to a lower throughput. A balance must be struck between resolution and sensitivity. In fact, for a lift off process, a higher sensitivity is desired since it promotes an undercut.

Electrons react with the resist via inelastic collisions. These types of collisions result in the ionization of the polymer that not only generate secondary electrons, it also results in physic-chemical changes in the polymer. Different tone resists can be used, like

in photolithography. Positive resists, such as PMMA, break down a long chain polymer into smaller, soluble fragments when exposed by the electron beam. Negative resist, such as hydrogen silsesquioxane (HSQ), undergo cross-linking, reducing the solubility of the exposed region. Once exposed, the resist is developed in a solution. Temperature and developing time are important with regards to the resolution. It is possible to do a "cold development" where the selectivity between the exposed and unexposed development is improved. Overdevelopment can result in mechanical instability of the resist that can cause pattern collapses.

Most of the processes done in this research are lift-off after metallization. We use a high voltage to maintain resolution, but to ensure lift-off a bilayer is employed. The first resist spun has a lower molecular weight, so it develops faster than the one above. In addition, since our Si/SiO2 substrate is prone to charging, we apply a thin chromium layer after the resist is spun in order to avoid any charge build up (Figure 3-5). While a single resist low voltage may be enticing, it also comes with other problems. The dose window with low voltage is very narrow, especially for high-resolution features. Small variations will significantly impact the output of the fabrication process. While cold-development can offset this problem, we have found it to be easier to do a bilayer process for small scale features.

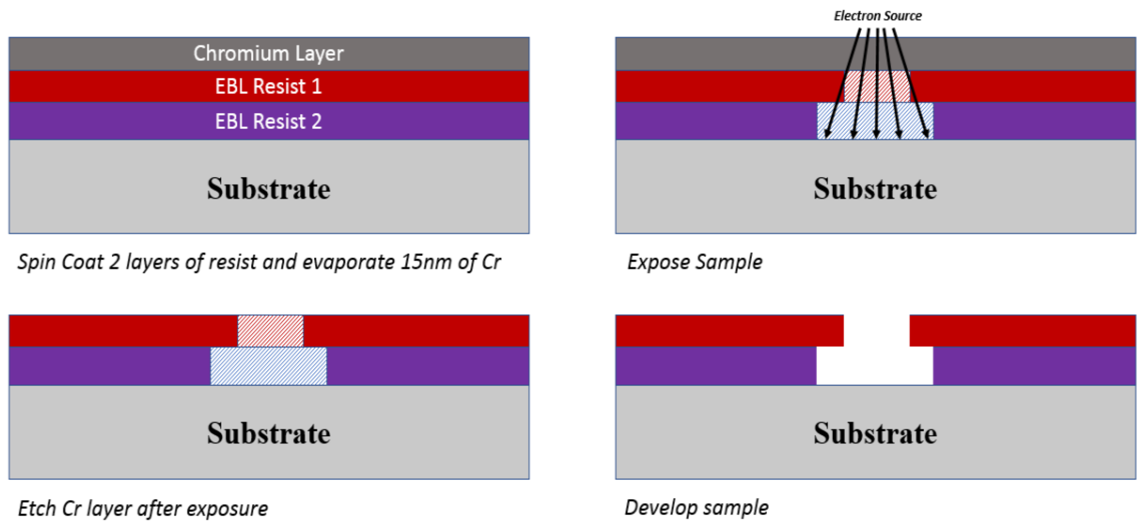

Figure 3-5: Two resist method demonstrating overhang for enhanced liftoff

There are many apparent advantages and disadvantages of EBL. While throughput is a major disadvantage, it is not of interest in this work. Our concern is being able to develop prototypes with small scale features. This research topic explores dimensions of MTJs that have remained unexplored. For industrial purposes, being able to produce a large array of small devices is critical, but in a research environment it is not necessary. EBL has been indispensable in this thesis, where much of the patterning has been done with this process.

The following recipe was characterized and used for EBL lift-off:

Table 2: EBL Bilayer Lift-Off Process (Positive Tone) Recipe

Dehydration Bake	Hotplate 5min/180°C
Spin Coat	Resist Thickness: 100nm Spin 1: 500 rpm Ramp 1: 250 rpm/s Time 1: 5 s Spin 2: 5000 rpm Ramp 2: 2500 rpm/s Time 2: 30 s
Soft Bake	Hotplate 3min/180°C
Spin Coat	Resist Thickness: 100nm Spin 1: 500 rpm Ramp 1: 250 rpm/s Time 1: 5 s Spin 2: 5000 rpm Ramp 2: 2500 rpm/s Time 2: 30 s
Soft Bake	Hotplate 1.5min/180°C
Cr Evaporation	Deposit 15nm
Exposure	170 $\mu C/cm^2$
Cr Etch	Etch in Chrome Etchant 1020 for 30s
Development	MIBK 1:3 to IPA, 60s
Descum	O_2 Plasma Etch for 60s

.

3.4. **Thin Film Deposition**

A thin film can range from a few angstroms in thickness to several microns. They are the building blocks in a wide range of applications, such as integrated circuits (IC), micro-electro-mechanical systems (MEMS), sensors, solar cells, magnetic media, LEDs, etc. They are also essential in the development of materials with unique properties, such as multiferroics. Films are usually deposited onto a substrate and are commonly done by either physical or chemical deposition techniques. Different techniques have certain advantages and disadvantages like material constraints, deposition rates, film quality, adhesion, deposition directionality, costs, etc. Devices developed in this thesis made extensive use of different thin film deposition techniques. These techniques will be discussed in further detail later in this chapter.

Thin films are deposited in a vacuum to ensure the removal of unwanted particles and impurities. This is done with a vacuum pump, where pressure differences cause gas and particles to migrate out of the chamber. The base pressure indicates the quality of the vacuum and by extension the quality of the films deposited. The higher the vacuum, the longer the mean free path (MFP) of unwanted particles. When pumping down a chamber, there are 3 flow regimes that require different pumps. The viscous flow has a pressure range from atmosphere (~760 Torr) to 10^{-2} Torr. In this regime gas molecules are very close and in constant motion. The distance they travel before collisions (MFP) is very short. Positive displacement pumps or "roughing" pumps are used to create physical pressure differentials, displacing the gas in the chamber. The transitional flow is ~10^{-3} Torr. As more molecules are removed the MFP increases, reducing the effectiveness of the roughing pump. Fewer molecules are removed with each cycle until there are too

few of them, changing the flow regime. Molecules at this point are more likely to collide with the chamber wall than with other molecules. The final regime is molecular flow, where the pressure in the chamber is smaller than 10^{-3} Torr. Molecules are randomly moving around, independent of other gas molecules, so pressure differentials are ineffectual. Special high vacuum pumps that operate on kinetic transfer or entrapment are used, such as turbo-molecular and cryogenic pumps. The MFP is directly related to the pressure [74] and can be calculated with the following formula:

$$MFP = \frac{k_B T}{\sqrt{2}\pi d^2 P}$$

The parameters k_B is the Boltzmann constant, T is the temperature, d is the diameter of the molecule, and P is the pressure.

Uniformity, purity, film density, stoichiometry, and roughness must be carefully monitored when developing recipes with the different film depositions. Process conditions such as gas composition, vacuum, purity of the materials, deposition pressure, are just some of the things to consider when depositing a film. Roughness is critical in the functionality of the devices developed in this thesis. For example, magnetic tunnel junctions require smooth films otherwise the performance degrades substantially. Depending on what is critical in the fabrication process, we must carefully choose and tune the appropriate film deposition techniques for this research.

3.4.1. **Physical Vapor Deposition**

Physical vapor deposition use physical means to deposit thin films onto a substrate. Typically, materials go from a condensed phase to a vapor phase, and back to a condensed thin film phase. Thin films coated via PVD methods tend to be harder and more corrosion

resistant. A wide variety of materials, both organic and inorganic, can be deposited on a wide variety of substrate materials. However, most PVD processes are "line-of-sight" and therefore directional [56]. This poses a problem if substrates or features with high aspect ratios or undercuts need to be coated. Cooling is also a problem since PVD processes tend to generate a lot of heat that needs to be quickly dissipated. The most common PVD techniques are evaporation and sputtering.

Evaporation deposition involves high temperatures to vaporize materials that condensate onto a substrate. The material to be evaporated is heated until it becomes gaseous and travels to the substrate. The material can either sublime (solid to gas) or evaporate (liquid to gas). Evaporation takes place in a vacuum, where the purity and uniformity of the deposited film increases with increased vacuum. Typically evaporation is done thermally, where a material is either joule heated in the cavity of a ceramic or placed in a crucible that is heated via radiation from an electric filament. Another common method uses electron beams with energies greater than 10keV. Electron beams are generated from thermionic emission, field electron emission, and anodic arc method [75], [76]. The electron beam should be generated in high vacuum to allow electrons to travel from the source to the target material. Typically a charged tungsten filament is used. In this thesis, electron beam evaporation is frequently used. The main advantages include a wide window of deposition rates that can be established. Materials can be deposited from a few nanometers a minute to several microns.

Sputtering is a plasma-assisted technique that involves bombardment of the depositing material with gaseous ions, such as Argon. A plasma is one of the four fundamental states of matter where an ionized gaseous substance becomes electrically

conductive due to a string electromagnetic field or by heating. Despite the generation of ions, a plasma is electrically neutral (total charge is zero). In a vacuum, a voltage is applied between the target (cathode) and the substrate (anode) and plasma is generated ionizing the sputtering gas (Argon) [56]. With the right conditions, including voltage bias and pressure, stable plasma can be maintained. These ions (Argon) are accelerated towards the depositing material, which eject atoms due to momentum transfer. Ejected material ballistically travel and condensate onto the substrate. Depending on the sputtering conditions, ejected material can have energies in the order of tens of eV. Higher gas pressure result in more collisions between ions and target material, resulting in more of a diffusive and conformal deposition due to random scattering [77]. The depositing material tends to condensate onto the substrate with less energy. Alternatively, less pressure results in more momentum transfer from the ions onto the substrate due to increased mean free path. Ejected atoms tend to have more energy, and the sputter process is more directional. In this thesis, magnetron sputtering was used. This type of sputtering uses a closed magnetic field to trap electrons [78]. This configuration improves the sputtering deposition process by enhancing the ionization process and allowing sputtering to maintain stable plasma at lower pressures.

Sputtering has several advantages over evaporation. Sputtered films tend to be of higher quality in terms of film density and smoothness since sputtered atoms have greater energies (over an order of magnitude) when coating a substrate. Because of this greater energy, they also tend to adhere better to the substrate also. Evaporation relies on the melting points of materials, making them unsuitable for alloys and compounds. Sputtering doesn't discriminate between materials, therefore stoichiometry is maintained. The sputtered process can be tuned for either a directional deposition or a conformal one. E-

beam evaporation, however, has a wider range of deposition rates and is a much more line-of-site deposition method than sputtering. Evaporation also deposits at much lower process pressures, therefore films tend to be purer than sputtered ones. Depending on what type of film or process the user is running, both evaporation and sputtering have advantages over each other. In this thesis, electrical contacts were typically evaporated, while the MTJ device was sputtered.

3.4.2. **Chemical Vapor Deposition**

While PVD involves physical methods to deposit films, CVD involves chemical processes to deposit thin films. Typically a substrate is exposed to volatile precursors that react and/or decompose onto the surface of the substrate. Any by-products are removed via gas flow through the reaction chamber. Gas or vapor is introduced into a chamber where the substrate is placed, and they move through the system evenly, across the surface of the wafer. The surface of the substrate absorbs the precursors and chemical reactions occur. These reactions tend to start off as islands and eventually spread across the wafer. Flow regulators and control valves are used to manage the gases and the reaction conditions. Typical CVD processes include low pressure chemical vapor deposition, used for depositing polysilicon, doped and undoped oxides, and nitrides. Plasma-enhanced chemical vapor deposition (PECVD) is a relatively low temperature CVD process. Low temperatures are compensated with the addition of plasma which provides energy from free electrons to assist in the reactions. Typical films grown are silicon oxides and nitrides, amorphous silicon, and silicon oxynitrides.

CVD isn’t commonly used in this thesis, but it is worth mentioning that they offer unprecedented advantages over PVD when conformal films or augmented substrate

surfaces are needed. However, many CVD processes typically run at much higher temperatures than PVD processes. Also, precursors and byproducts tend to be hazardous, and a challenge to handle and store. The temperatures and gases would create problems with the process flow intended for MTJ devices. Furthermore, PVD processes are better characterized in the lab than CVD ones. Atomic layer deposition (ALD), however, is a promising CVD process that has the capability to deposit uniform monolayers onto a substrate by inserting gases as a series of sequential pulses [79], [80]. Thin film growth at the atomic level would prove useful for depositing ultra-precise insulating layers in the MTJ. This could improve the overall performance of MTJs. Costs of an ALD system remain high, intensive characterization is required for optimal film quality and control, and the deposition rate is really slow (1-5nm/min).

3.4.3. **Electroplating**

Electroplating involves the use of electric current to reduce metal cations to form a metal coating on an electrode. A sample is submerged in a coating solution and direct current is applied using electrodes. The coated object is one of the electrodes and a counter electrode is used to complete the circuit. Voltages can range between 20-400V. This process can be either anodic or cathodic, depending on the charge of the material and electrode. Once a field is applied, the charged material migrates towards the oppositely charged electrode via electrophoresis [81]. The material is deposited either by charge destruction which results in a decrease of solubility, concentration coagulation, and salting out. The coatings have the advantage of being uniform and without porosity. Given the conformal nature of this technique, complex geometries and cavities can easily be coated. Thick films can be coated relatively fast and with comparatively low costs. In this thesis,

electroplating was done to create nanowire contacts in nano-porous alumina. The idea was to create a long ohmic contact from the top of the alumina disk where the MTJ device was sputtered to the grounding plate at the bottom of the disk.

4. EXPERIMENTAL RESULTS

4.1. Motivation and Introduction

Demand for energy efficient computation is increasing with the growth of the emerging fields of the internet of things (IoT), large scale sensor networks, neuro-inspired computation, bioelectronics, etc. Current technology is reaching its upper limits of impact in terms of computing and memory storage capability. This limit is defined by fundamental physics which is forcing researchers and engineers to innovate and explore new areas of quantum physics to overcome current limitations. Another key motivation stems from the increase in power cost. We live in the information age where there has been rapid growth in cloud computing and social networking (among many other related topics) consuming approximately 1.4% of the world's electricity [82]. This energy is needed to fuel the massive data centers and servers and is expected to continue to grow. Landauer defined the minimum energy to manipulate a bit of information at $kT*\ln 2$, which is over 100,000 less energy than what is used in modern semiconductor-based transistors [83].

Non-volatile memory with novel computing mechanisms are prominent fields being explored to replace current semiconductor technology. Theoretically spintronics is a leading candidate due to its inherent non-volatility (magnetic), potential low voltage and high-speed computational operation, long lifespan, scalability in the sub-5nm range, multilevel integration, very low power consumption, radiation hardness, and much more. The overall concept is the manipulation of nanomagnets for reading and writing operations. Memory states are interpreted according to different levels of resistance governed by the relative change in tunneling magnetoresistance (TMR). Writing can be achieved by different mechanisms such as the application of an external magnetic field, spin-transfer

torque (STT), spin-orbit torque (SOT), etc [84]. While much progress has been made in this field, there are two main challenges that must be addressed: reducing the energy required to switch magnetic states and increasing the tunneling magnetoresistance (TMR) to an acceptable on/off ratio. This thesis addresses these challenges first hand and explores novel experimental methods to understand aspects of the field of spintronics that remains poorly understood.

4.2. Magnetic Tunnel Junction

It is noteworthy that the GMR or TMR effect in spintronic devices is equivalent to the On/Off ratio in CMOS devices. Spin transfer torque based logic devices remain leading edge candidates as an alternative to CMOS. Currently these devices are implemented as read-heads in magnetic hard drives. They operate utilizing the TMR effect and the basic architecture is that of a tunnel junction: 2 ferromagnetic thin films separated by a thin insulator. This thin film configuration is known as a magnetic tunneling junction (MTJ). Classically, electrons cannot conduct through the insulating barrier, but if it is thin enough, they can tunnel through according to quantum mechanics [85]. The resistance across the junction depends on the relative magnetic orientation of the ferromagnetic layers. When they are aligned in parallel, the resistance is low, otherwise the resistance is high (antiparallel). This TMR effect was discovered by Jullière in 1975 when he experimented with Fe/GeO/Fe junctions at low temperatures [13].

Jullière explained this phenomenon operating under the assumption that spin orientation is conserved across the tunnel barrier; there spins can only tunnel into a band with the same spin orientation. The tunneling current therefore depends on the density of states of the 2 ferromagnetic layers as illustrated in Figure 4-1. When both ferromagnetic

layers are aligned, electrons will go from a majority band to majority band, and minority band to minority band with minimal scattering. When they are misaligned, however, minority band electrons will conduct to majority bands while majority band electrons to minority bands, increasing scattering (higher resistance). The magnetoresistance is expressed as the relative resistance change between the parallel and antiparallel state between the 2 ferromagnetic layers:

$$TMR = \frac{R_{\uparrow\downarrow} - R_{\uparrow\uparrow}}{R_{\uparrow\uparrow}}$$

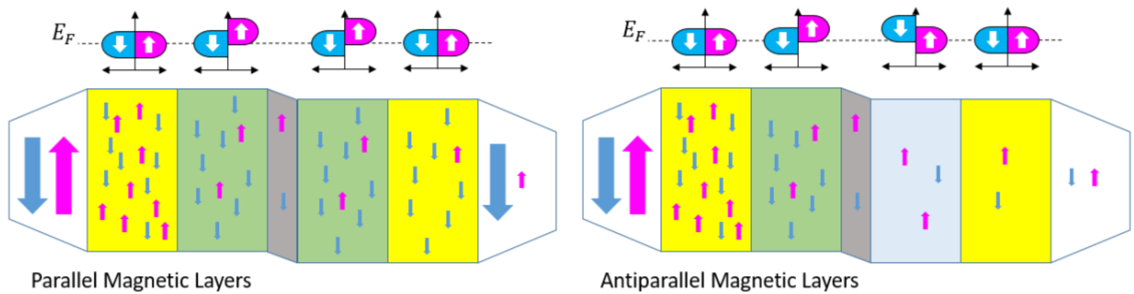

Figure 4-1: Illustration of MTJ "ON" state, parallel (left) and "OFF" state, antiparallel (right)

According to Jullière's model, magnetoresistance can be calculated from the spin polarization. Polarization is computed according to the spin dependent density of states:

$$P = \frac{D_1(\uparrow) - D_2(\downarrow)}{D_1(\uparrow) + D_2(\downarrow)}$$

Because magnetoresistance depends on the relative orientation of the ferromagnetic layers, according to the Jullière's model it can also be expressed according to the relative polarization of each ferromagnetic layer:

$$TMR\ (\text{Jullière}) = \frac{2P_1P_2}{1 - P_1P_2}$$

Increasing the polarization of the ferromagnetic layers increases the overall TMR. With 100% polarization (Figure 4-2) an infinite TMR is possible, creating a near perfect switch! Film quality and understanding interfacing properties between films is critical for obtaining high TMR. There are also materials currently being studied with high spin polarization called ferromagnetic half metals [86]. Increasing TMR is an important area of study in spintronics.

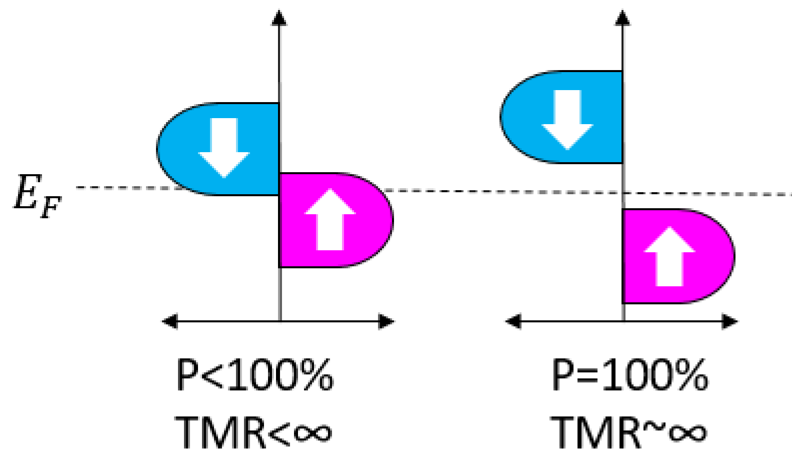

Figure 4-2: Polarization levels in ferromagnetic layers corresponding to non-infinite and infinite TMR

Spin transfer torque (STT) is the switching mechanism that manipulates the magnetic orientation of the magnetic layers in an MTJ [87]. A spin polarized current can transfer enough angular momentum to a ferromagnet to switch its direction of magnetization. In an MTJ, an unpolarized current (equal amount of spin-up and spin-down electrons) passes through a ferromagnetic layer, polarizing the current. This current then passes through the second ferromagnetic layer exciting oscillations and eventually flipping the magnetic state with enough applied current. STT switching is observable only in

nanometer scale devices and has theoretical advantages of low power consumption and scalability when switching magnets as opposed to external magnetic fields [88]. While this technology is currently implemented in MRAM (magnetoresistive random access memory) and utilized in a niche market, the switching current remains too high for broad commercial applications [89].

In an MTJ, one of the ferromagnetic layers are typically magnetically hard or "fixed", while the second one is magnetically soft or "free". Switching occurs in the free magnetic layer using STT. Switching dynamics are best described by the Landau-Lifshitz-Gilbert (LLG) equation [90]:

$$\frac{dM_{soft}}{dt} = \gamma\left(M_{soft} \times H_{eff}\right) - \alpha\left(M_{soft} \times \frac{dM}{dt}\right) + \beta J\left(M_{soft} \times M_{hard}\right)$$

The spin precession around the effective field is described in the first term. The effective field is the sum of the external magnetic field, anisotropy field, exchange field, etc. The second refers to the energy loss decreasing the precession angle. The final term takes into account STT describing the switching mechanism. The coefficient β is a STT term that actively competes with the dampening term α. With enough current density the magnetic oscillations can excite allowing it to precess at larger angles as illustrated in Figure 4-3.

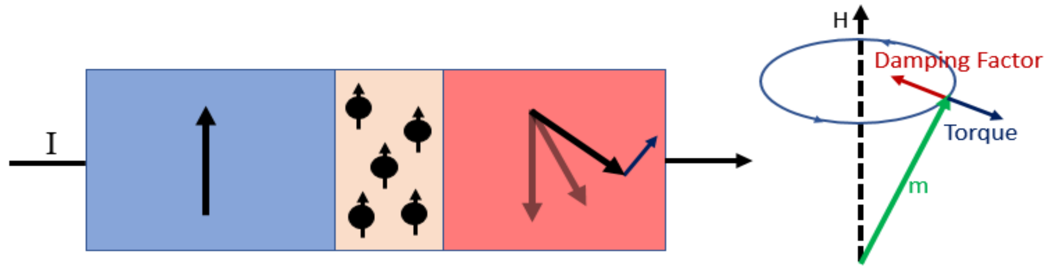

Figure 4-3: Spin transfer torque forces acting on precession

Above a critical current, the spin torque can dominate the precesional behavior and switch the magnetization direction [91], [92]. Both the direction and magnitude of the switching current affects the ease at which a magnet changes magnetization direction. In an MTJ to switch from antiparallel to parallel current conducts from the fixed layer to the free layer. From parallel to antiparallel, current should flow from free layer to the fixed one as illustrated in Figure 4-4.

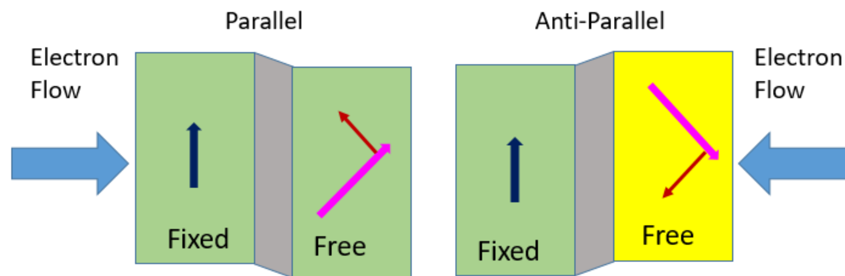

Figure 4-4: Spin transfer torque effects due to direction of spin-oriented electron flow

Scalability is one of the key advantages of STT based MTJs as demonstrated in the following chapters.

4.3. **Justification for sub-10nm STT-MTJ device fabrication**

This thesis focuses on developing novel fabrication methods to create vehicles to understand the physics of spintronic devices in the sub-5nm range. It was hypothesized that reducing the size of MTJs below 5nm allows for quantum mechanics to dominate the physics of the device in correlation with surface vs volume effects [93]. This intermediate size regime diverges from the traditional continuous crystal lattice model and mitigates the effectiveness of thermal reservoirs to absorb magnetic excitation energy. A cluster of atoms is a more accurate representation of this size regime where energy exchange is less effective than in a continuous crystal. The combination of the aforementioned conditions increases spin excitation lifetime due to decreased magnetization dampening. Thus increasing the switching efficiency substantially to the point where anomalous magnetotransport effects can be present at room temperature.

4.3.1. **Atomic clustered quantum mechanical simulation**

Based on the hypothesis that sub 10 nm clusters would maintain spin cohesion longer than continues crystal models, numerical analysis has been done by Khizroev *et. al.* simulating the kinetics of spin excitations in cubic nanomagnets (Figure 4-5). Two size ranges were studied: 2nm and 15nm. They are both initialized in a state where spins were co-aligned. A reversal field is applied to both magnets to trigger a relaxation process.

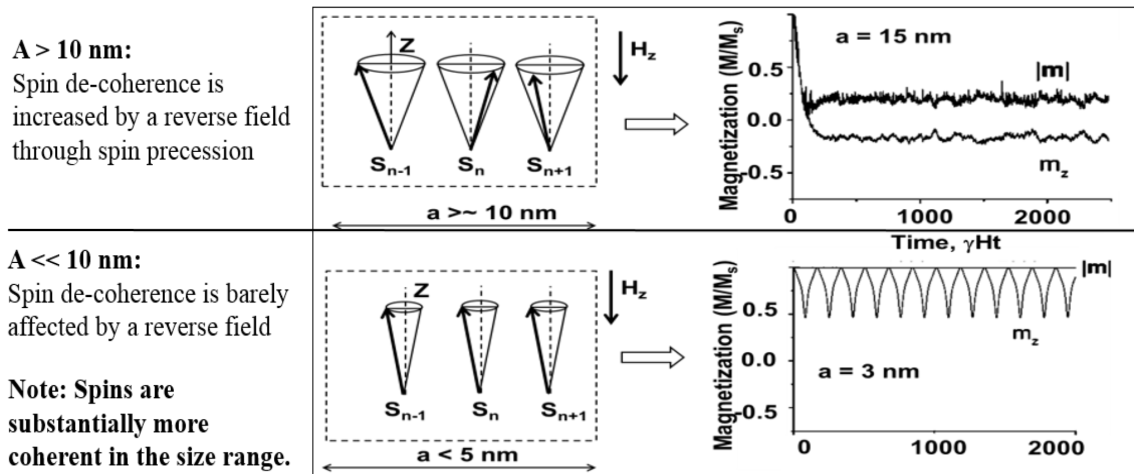

Figure 4-5: Quantum mechanical simulations illustrating de-coherence above 10nm and coherence below 5nm vs time [94]

For the 15nm cluster the relaxation process occurred via a spin precession where spins become de-coherent over time. In the 2nm cluster, however, coherence between adjacent spin was not broken due to a relatively slow relaxation process and minimal dampening. This simulation motivated the pursuit to study nanoscale spintronic devices experimentally.

4.3.2. AFM experiment

To test the theoretical simulation above an Atomic Force Microscope (AFM) tip was used as a substrate to deposit a typical MTJ stack using sputter deposition. The films consisted of Ta(5 nm)/CoFeB(1 nm)/MgO(0.9 nm)/CoFeB(1 nm)/Ta(5 nm) then the tip was further sharpened using a Focused Ion Beam (FIB) to reduce the diameter of the tip to approximately 10nm diameter (Figure 4-6).

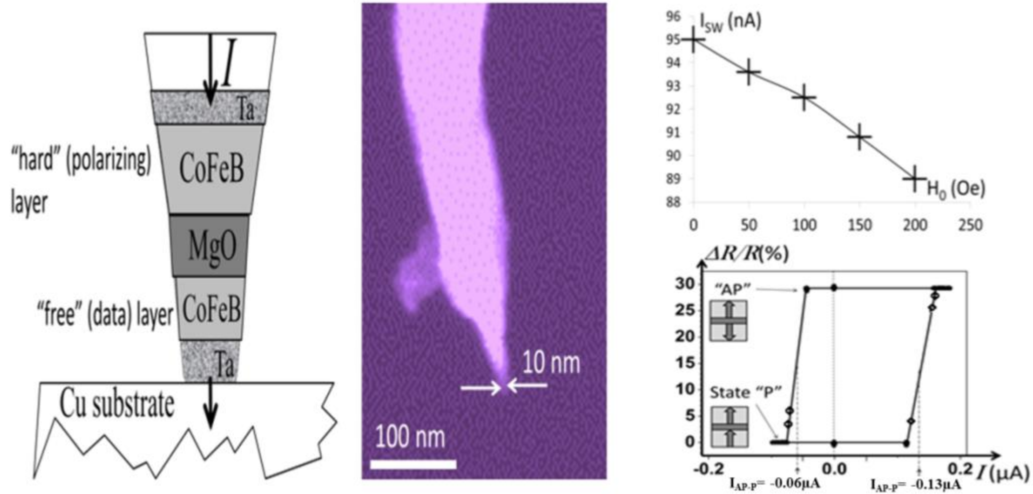

Figure 4-6: Illustration of MTJ stack on modified AFM tip (left), SEM of modified AFM tip (middle), switching current vs applied magnetic field (top right), and current vs resistance loop (bottom right) [95]

Two extremely important physical phenomenon were observed. 1) As an increasing external magnetic field is applied the current required to switch magnetic states decreased and 2) the IR curve indicated a 30% change in Magnetoresistance (MR).

4.3.3. **FIB-MTJ**

In order to continue investigating Sub-10nm theory, additional fabrication experiments were carried out in which the lower limits of photolithography was used to fabricate the MTJ stack as illustrated in chapter 3, figure 3-1 using the same thin film stack as above Ta(5 nm)/CoFeB(1 nm)/MgO(0.9 nm)/CoFeB(1 nm)/Ta(5 nm). These relatively large micron structures were placed in a FIB and milled away until the area of the device was reduced in steps down to 5nm (Figure 4-7).

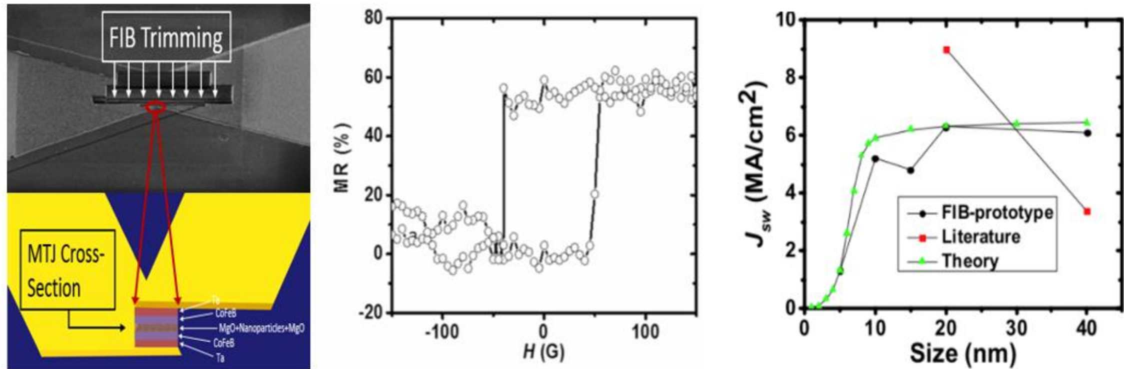

Figure 4-7: SEM of trimmed MTJ stack (top left), device rendering (bottom left), MR loop (middle), and experimental trending with theoretical switching current vs device size (right)

Two very significant results from this experiment was 1) in the 5nm sample the MR was 60%, twice that of the modified AFM tip experiment and 2) the switching current followed that of the simulated curves figure 4-7 right [95].

4.4. Current Contributions to State of the Art

4.4.1. Nanoparticle MTJ

One set of devices developed in this thesis were dual magnetic tunnel junctions embedded with magnetic nanoparticles, dubbed "Nanoparticle-MTJs". These structures were essentially traditional MTJ devices as illustrated in figure 3-1 and directly above with the added ~2nm nanoparticles sandwiched in the tunneling barrier. This alternate bottoms-up method was proposed to counter the challenging top-down methods that utilize size limited patterning techniques (photolithography, electron-beam lithography, focused-ion beam, etc.). Nanoparticles are a promising contender for mass producing spintronic devices because of the well-established chemical procedures that can synthesize them in the sub-5nm range with high uniformity in both size and composition. The exact device

composition consists of 2nm $CoFe_2O_4$ nanoparticles sandwiched between two 1-nm thick MgO layers which are also sandwiched between 1-nm thick CoFeB-based ferromagnetic layers and 5nm Ta layers illustrated in Figure 4-8.

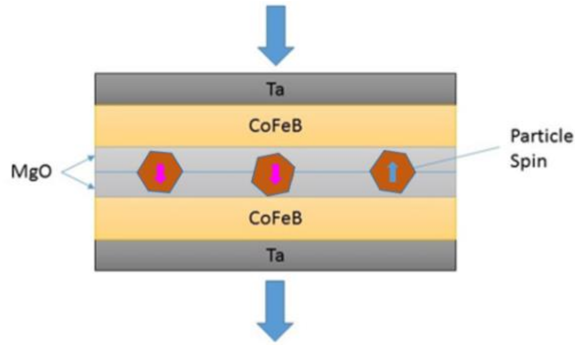

Figure 4-8: Cross section of pinned sub-5nm particles in magnetic tunnel junction stack

MTJ thin films were deposited via sputtering where roughness was measured using atomic force microscopy (AFM) and the deposition rate characterized with profilometry. Ferrimagnetic $CoFe_2O_4$ 2nm nanoparticles, synthesized with a chemical process (co-precipitation), were deposited onto the first sputtered MgO layer. The nanoparticles were suspended in hexane solution and deposited manually with a dropper. The second MgO layer was sputtered to separate the nanoparticles from the top CoFeB film. Magnetic force microscopy (MFM) was conducted to verify the magnetic nature of the particle, and the nanoparticles' crystallinity was verified through high-resolution TEM. Photolithography was used to define the initial device size (~20umx20um) and trimmed further with a focused ion beam (FIB). The purpose of trimming was to increase the odds of having a device with uniform thickness and to eliminate any apparent areas of particle aggregation.

FIB also allows quantifying the results with greater ease by reducing the nanoparticle count per device.

Measurements were done with a Keithley 2450 sourcemeter in a 4-point electrical contact orientation at room temperature with current sweeps in both the negative and positive directions. For magnetoresistance measurements, the Keithley sourcemeter was also used in conjunction with Helmholtz Coils for electrical resistance measurements. This allowed for relatively fast sweeping low magnetic fields up to 200 Oe, with a characteristic time constant of t=100ms.

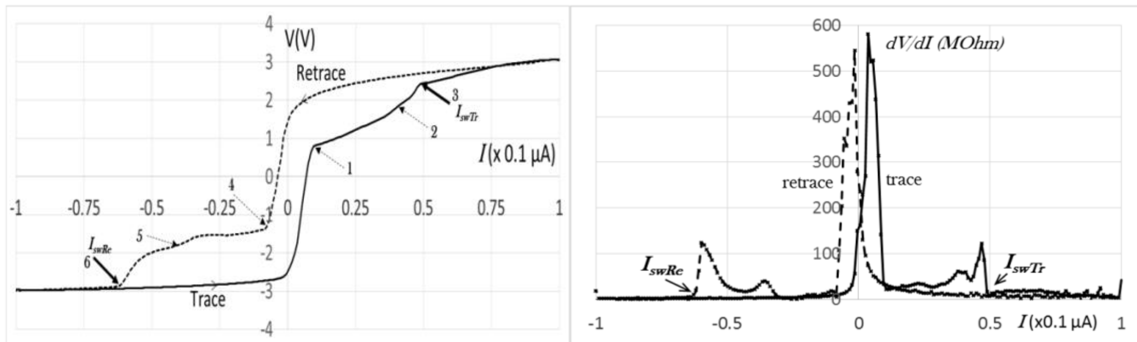

Figure 4-9: V-I curves for trace and retrace current directions. The characteristic Coulomb staircase steps are shown by thin arrows and marked by numbers 1 and 2 for trace and 4 and 5 for retrace. The STT switching currents are shown by thick arrows. The STT switching currents are marked as 3 and 6 for trace and retrace, respectively. (left) dV/dI-I curves for trace and retrace current directions (right)

From the IV curve (Figure 4-9) it would appear that one polarity describes Coulomb Blockade (CB) where a coulombic staircase is repeatedly observable. There are changes in the relative magnetization orientation throughout the sweep which are best described in the following Figure 4-10:

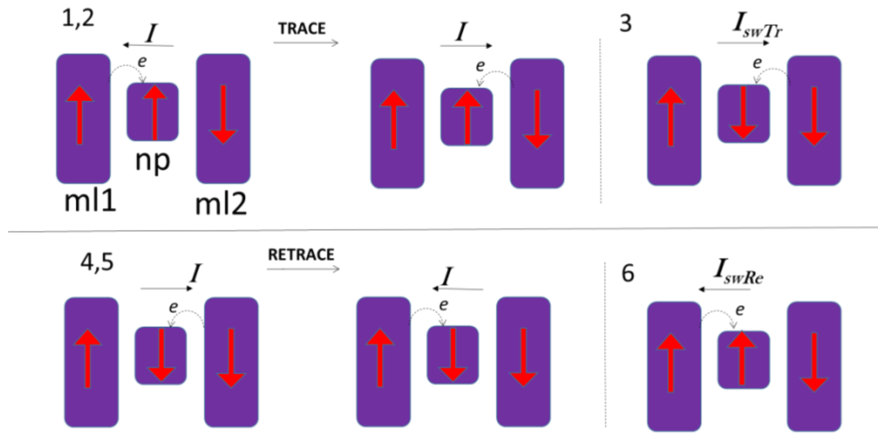

Figure 4-10: Illustration of nanoparticle magnetization switching with respect to Fig. 4-9 V-I curve in chronological order

Due to the dominant shape anisotropy, the magnetic layers are aligned in plane rather than out [41]. The relative orientations could be forced into an anti-parallel state via an AC demagnetization from a decaying AC field oscillating at 60 Hz. To ensure the antiparallel state of the 2 thin film magnetic layers (CoFeB), the applied magnetic fields didn't exceed 100 Oe, allowing only the nanoparticle magnetization to switch directions.

Experiments were also done with full-loop low-field magnetoresistance (MR) dependences of the Particle-MTJ with a magnetic field applied perpendicular to the film plane for two critical current values: 0.01 and 0.05 uA. These current values were chosen as two key points in the staircase dependent IV sweep where for I = 0.01uA corresponds to the first resistance change and I = 0.05uA to the second. For I = 0.05uA, relatively reversible MR oscillations were observed with a characteristic field separation between adjacent resistance slumps in the order of 20 Oe (Figure 4-11). This could be due to shifts in the Fermi energy from the application of the external magnetic field. The applied magnetic field shifts through the nanoparticle's discrete energy levels much in the same way an electric field would in the traditional coulombic blockade staircase.

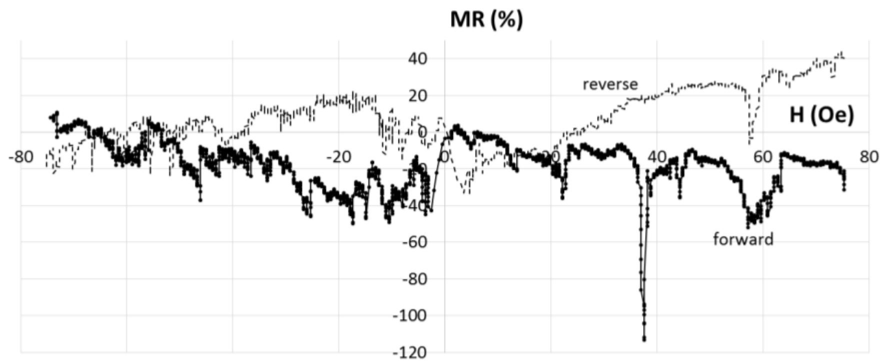

Figure 4-11: MR curve of nanoparticle-integrated STT-MTJ device at 0.05uA bias current

For I = 0.01uA, however, there was no sign of reversible dependencies (Figure 4-12). This could be due to how "close" this current value is to the resistance change below the switching threshold. The data was taken with a characteristic measurement time constant of 1ms. It is also worth noting that for fields greater than 100 Oe, no oscillatory effects were observed for either current value. This supports the idea that to observe these effects, the relative alignment of the two ferromagnetic thin films must remain antiparallel.

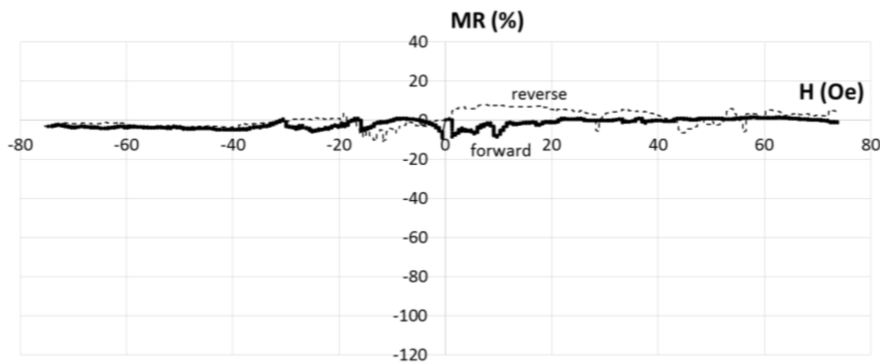

Figure 4-12: MR curve, 0.01uA bias current nanoparticle-integrate STT-MTJ device

This innovative design turns a traditional MTJ structure into a device containing an array of dual junctions with single-electron transport capability. It is important to note that the traditional Coulombic staircase that stems from single electron transport is expected to be symmetric across the IV sweep for non-magnetic dependent structures [96]. In this case however, due to the presence of the ferromagnetic layers the coulombic staircase is only present for either the positive or negative swing of the IV trace. This may be due to the dependence between the nanoparticles relative magnetization direction with magnetization direction of the thin films. When keeping the ferromagnetic thin films magnetization fixed, the coulombic staircase becomes very apparent as opposed to when we apply stronger magnetic fields that switch the magnetization direction of these same films. The nanoparticle can switch between the 2 antiparallel states via the STT effect so long as the thin films remained fixed. The interaction between each incoming electron and the electron at the nanoparticle is affected by the relative orientation of the nanoparticle and thin film magnetization. The magnitude of coulombic repulsion between the two electrons can be manipulated based on the relative magnetic orientations due to spin-dependent exchange coupling. The coulombic blockade will be stronger (and therefore easier to generate a staircase dependence) for parallel spin orientations than antiparallel ones because of the higher energy required to push an electron sitting at the nanoparticle towards the layer receiving the electron. Switching occurs at higher currents (0.01uA and 0.05uA comparison) since enough switching current density satisfies the condition for magnetization reversal [41]. For a 2nm particles we would ideally have a 4nm^2 cross-sectional area and therefore a switching current density of $5x10^{-8}A/4x10^{-14}cm^2= \sim 10^6$

A/cm^2, a value expected for devices in this size regime. This staircase dependency is repeatable for each IV sweep direction. This device was able to achieve an MR of 120%.

4.4.2. Stacked 3D Structures and Results

Due to their scalability and energy efficiency, spintronics has the promise of 3D integration. An experiment was done to demonstrate the capability of this facet by developing multilevel 3D structures. This extra dimension significantly improves the device footprint compared to traditional planar CMOS based devices. Sub-20nm MTJ devices were fabricated via FIB using He and Ne ion sources and tested via traditional magnetotransport methods [41], [45].

A tri-layer MTJ was fabricated intending Spin Transfer Torque (STT) as the switching mechanism between multi-level states where two junctions provide three resistance values. Previously, sub-10nm MTJ have been experimentally shown to switch at low switching current densities. The switching current density, J_s, can be expressed with the phenomenological expression:

$$J_s \sim M_s t \frac{\alpha}{p\xi}(H_{Keff} \pm H_0)$$

H_{Keff} is the anisotropy field that includes both intrinsic and shape anisotropy, H_0 is the net external field, α is the damping constant, ξ is the spin torque efficiency factor, M_s is the saturation magnetization (500 emu/cc), and t is the thickness of the "free" layer (1nm), p is the spin polarization, which is directly related to the magnetoresistance, $\Delta R/R$, according to Jullière's model.

The MTJ structure was fabricated via standard nanofabrication techniques illustrated in figure 3-1 but with additional layers. Using the focused ion beam (FIB)

trimming the size of the junction was in the order of 17nm (+/- 2nm). To induce perpendicular magnetic anisotropy (PMA), well-established Ta/CoFeB/MgO stacks were used. For increasing interface anisotropy of the second magnet, 2 stacks of MgO were deposited. The total film composition of the MTJ for this experiment was: Ta/Ru/Ta/CoFeB(M_1)/MgO/CoFeB(M_2)/MgO/CoFeB(M_3)/Ta. To vary the coercivity between the three magnetic films, they had different sputtering conditions and interface layers (coercivities for the trilayer were: 20Oe, 40Oe, and 60Oe (Figure 4-13 left)) [97]. This thin film configuration allows for ternary information processing. Field applied magnetic force microscopy (FA-MFM) was used to detect the 4 different signal levels (top right of Figure 4-13) as each magnetic layer was switched sequentially.

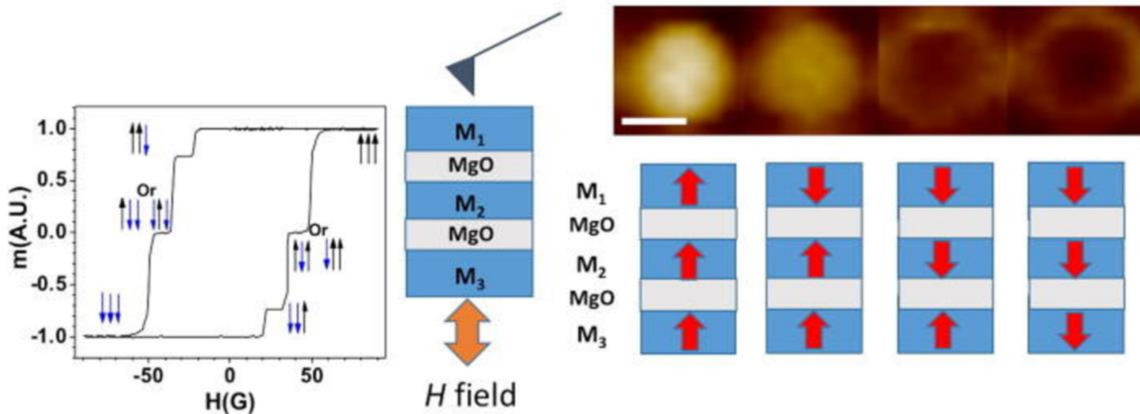

Figure 4-13: m-H loops of stack (left), MFM images and corresponding switching states due to applied field (right)

The total resistance of the MTJ depends on the TMR effect across the 2 junctions. Resistance values change according to the relative magnetization direction of each ferromagnetic layer. Switching of the magnetic layers can be done with current via the STT effect. With this device architecture 3 values of resistance can be extrapolated (Figure 4-14). With 8 different spin orientations possible in this device, 3 distinct relative

orientations can be observed: 1-All parallel (P-P) which corresponds to the lowest possible resistance; 2- Parallel and antiparallel orientation (P-AP and AP-P) corresponding to an intermediate resistance value; 3-Both antiparallel orientations (AP-AP) corresponding to the highest resistance value.

The following IV curve has three very obvious resistance changes expected from a dual junction device. The curve was obtained by sweeping the voltage from 0 to +100mV, +100mV to -100mV, and finally -110mV back to 0. The three resistance values were: 46kΩ, 52kΩ and 82kΩ. Based on the size of the device, the current density was calculated to be ~3MA/cm^2, a value that is comparable for standard MTJs of this size [95], [98]–[100].

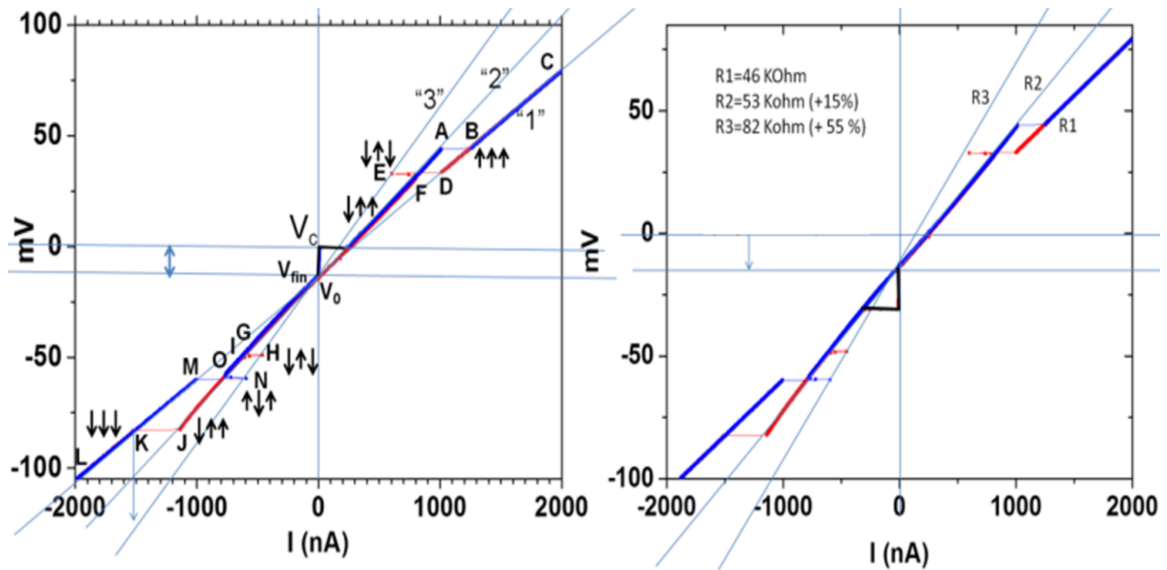

Figure 4-14: I-V measurement data of the stacked 3D structure annotated with possible switching mechanism (left) and the three corresponding resistances (right)

This experiment demonstrated the capability of multilevel logic in spintronics. The different magnetic films were capable of switching individually with the STT effect. This opens the door to the possibility of adding more junctions and adding more levels of logic.

This multilevel signal processing has already found applications in 3D electronics, process-in-memory (PIM), memristors, etc. There is also the capability for semiconductor integration for hybrid CMOS-spintronic devices.

4.4.3. Novel Approach to Mass Sub-10nm Device Fabrication

In the previously reported MTJ devices fabrication has been extremely difficult in the sense of low device yield which reduces the probability of successful measurements. Low device yield has to do with the difficulty in fabrication techniques as well as time consuming steps such as FIB to reduce the size of devices below 10nm approaching our theoretical critical dimensions in which Quantum effects dominate the system. Reported below is an architecture which permitted mass fabrication of devices in the order of billions per square centimeter.

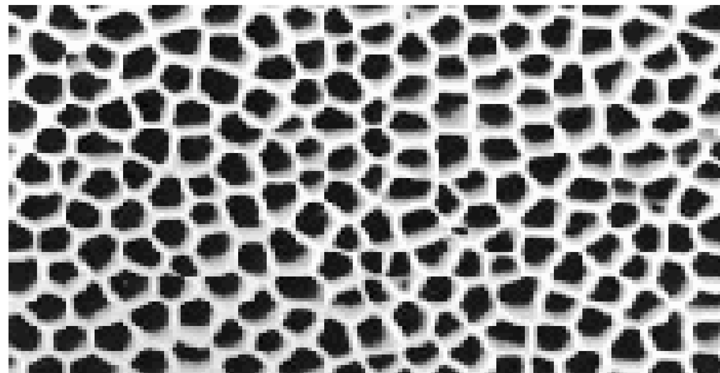

Figure 4-15: SEM of 0.02μm aluminum oxide membrane anodic disk

https://www.2spi.com/item/a0113-mb/

Commercial nanoporous anodic discs (Whatman WHA68097003) with pore diameters ranging from 20-80 nanometers were purchased and have been used as a

bottoms-up method for reducing the size of the MTJs. Figure 4-15 is an SEM image of the surface of their porous alumina discs.

Each alumina disk (Figure 4-16a) experienced a gold deposition in the order of 200nm thick intending to plug the pores and make a continuous backside electrode (Figure 4-16b). The disk was placed in a custom jig designed for electroplating[101] these extremely brittle disks. Figure 4-16c illustrates the electroplated wires. Copper electroplating was chosen due to its conductivity and its stability when introduced to gold etch solution. After electroplating copper through the pore to make nanowires the anodic disk had to be Chemically Mechanically Polished (CMP) to remove excess copper plated on the surface of the anodic disk. Figure 4-17 is an SEM image of the surface after CMP process in which the surface of the wires can be seen (white dots) and length portions of the wires can be seen on the broken edge (right side of the image).

Figure 4-16d shows the Gold etched away with Transene gold etch. Once the gold was etched away, the same surface of the anodic disk was introduced to a copper etch solution to recess the wires 20-50 nanometers also depicted in Figure 4-16d. This recession of the wires permits discontinuities of subsequent thin film depositions from the surface of the alumina disk to the surface of the nanowires creating discrete devices on the nanometer levels without lithography!! The same MTJ stack with particles, reported above, in our previous device illustrated in Figure 4-8 was deposited (Figure 4-16e). Then a 150nm copper layer was deposited to finalize the device to act as a common electrode for all of the STT-MTJ devices (Figure 4-16f). This common electrode can now be pinned against a metallic plate electrode protecting the devices while the other side of the 100um thick

anodic disk (copper wires only) can be probed without the probability of damaging the thin film stack.

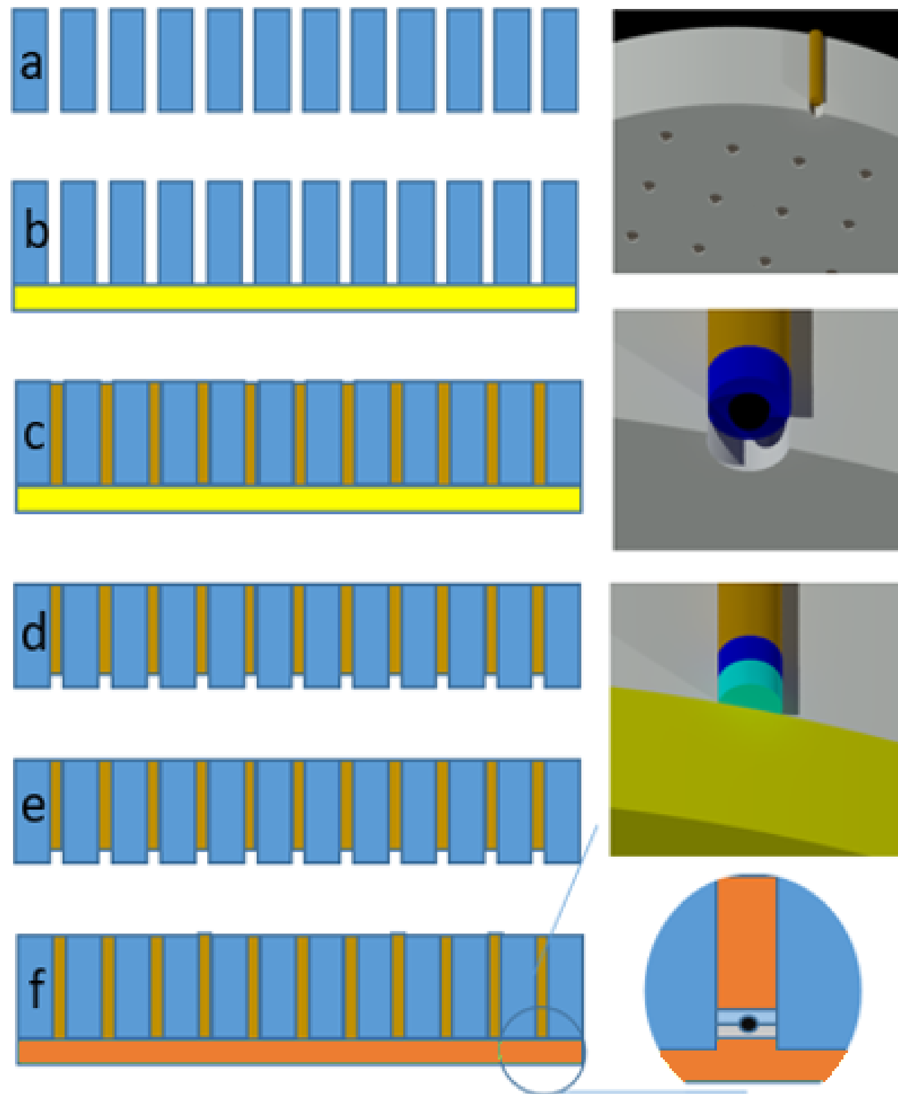

Figure 4-16: Cross section of fabrication process in nanoporous alumina: a) nanoporous alumina, b) gold evaporation, c) copper electroplating, d) gold etch, e) MTJ stack deposition, and f) copper evaporation of common electrode (inset: blowup of final device in one nanopore)

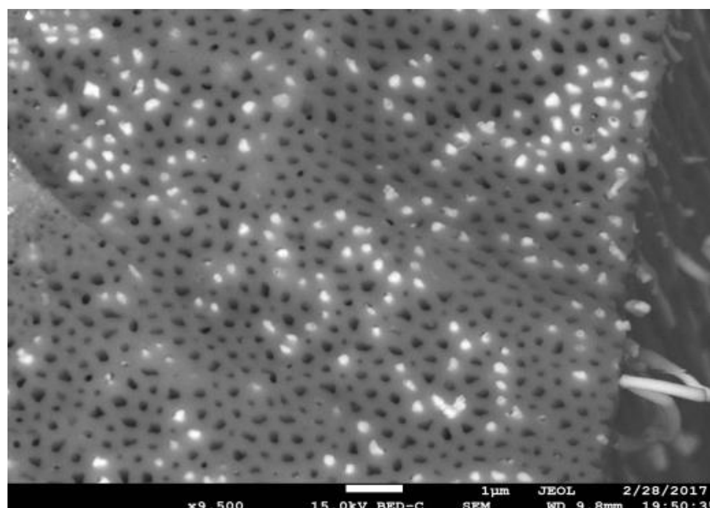

Figure 4-17: SEM of anodic disk with copper electroplated wires

Couple this architecture with the particle size distribution ranging from sub 1nm to 5nm and the controlled distribution of particles over a square area (Figure 4-18) allows us to limit a countable number of particles per pore in a non-destructive manner, i.e. FIB. Add to that the minor variation of deposited film thickness inherent to sputter deposition across the 13mm diameter anodic disk, permits vast combinations all within the tightly bound hypothesized size regime, defined by the theoretical model in Figure 11-7, for dominant quantum mechanical behavior. To adapt an analogy from Einstein, instead of hunting birds by shooting in the dark in a place that doesn't have many birds, we entered a completely filled bird atrium in the dark with a shotgun, after firing we felt around on the floor for things that felt like birds. It should be noted that we do not condone the actions described in the analogy however the concept is very well conveyed.

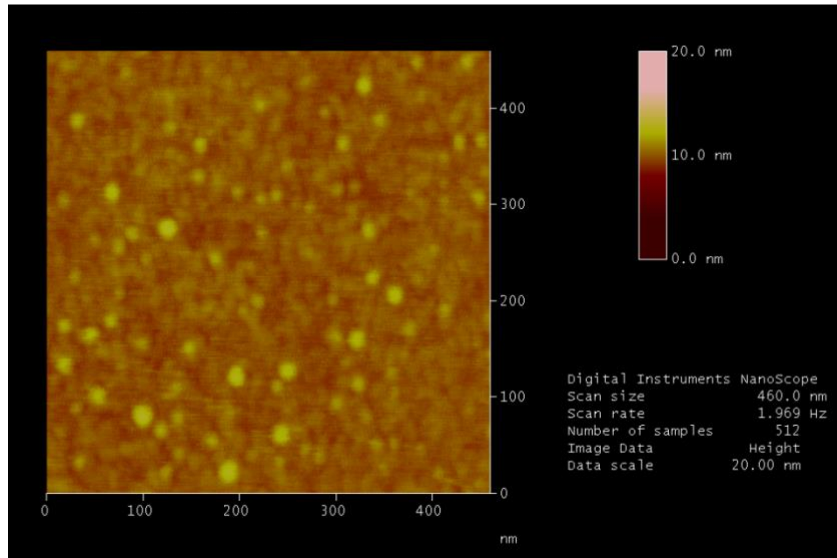

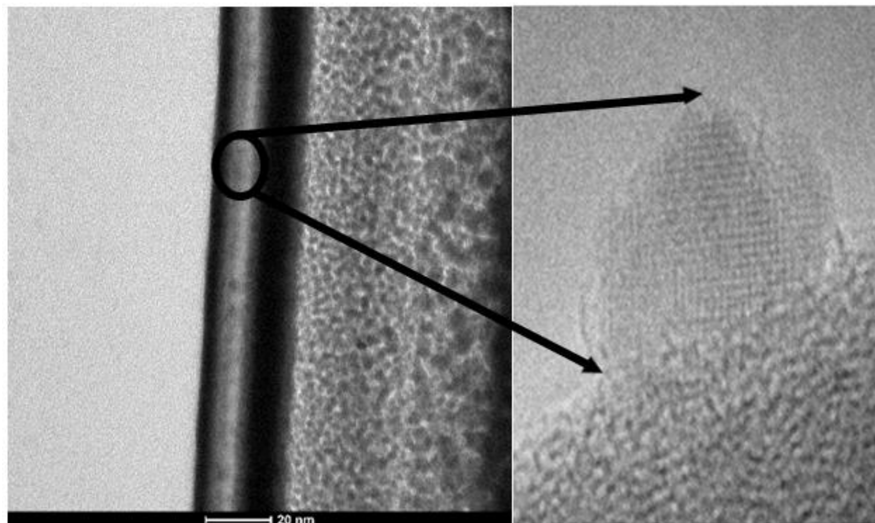

Figure 4-18: MFM size and space distribution of nanoparticles (left), TEM of MTJ stack with embedded nanoparticles (middle) and zoomed in TEM of single nanoparticle (right)

Resistance vs time experiments were done on these devices with different magnetic fields applied. Figure 4-19 shows 3 samples of data sets where current of I=10nA was applied for 3 different magnetic fields H=0T, H=0.3T and H=0.6T.

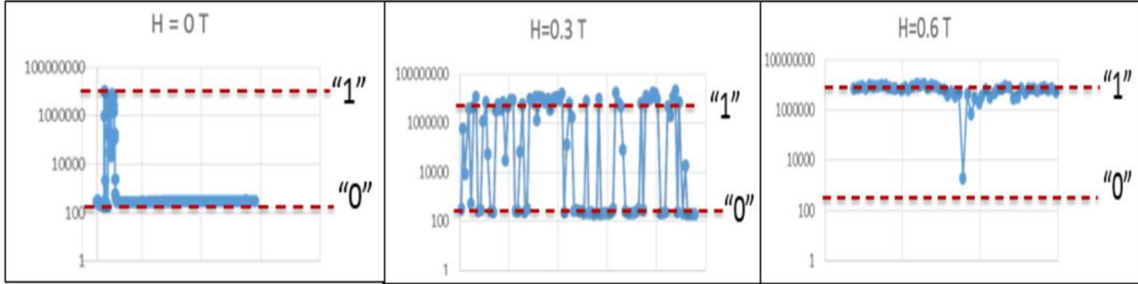

Figure 4-19: Resistance vs time with varied applied magnetic field using a 10nA current

It is apparent from the data set that there is a correlating dependency between the resistance and the applied magnetic field. In the absence of a magnetic field most of the resistance measurements linger around the order of 10^2 ohms. When a saturation field is applied (H=0.6T) resistances are in the order of 10^6 ohms. When an intermediate field is applied the values oscillate substantially between 10^2 ohms and 10^6 ohms. There is a definite quantum-like magnetic field dependency where the quantum mechanical mode and state are defined by elements of probability. There is an energy barrier where the applied magnetic field defines what state the device rests at with respect to it. According to Jullière's model [13], we can achieve an infinite TMR, which is becoming even more evident with the results illustrated in Figure 4-19. Using the TMR equation above Figure 4-1:

$$TMR = \frac{R_{\uparrow\downarrow} - R_{\uparrow\uparrow}}{R_{\uparrow\uparrow}}$$

We calculate the TMR for this device by allowing $R_{\uparrow\uparrow}$ = average low resistance in the on state and $R_{\uparrow\downarrow}$ = to average high resistance in the off state relative to the date represented in Figure 4-19. Doing so the TMR is approximately: 50,000% MR!!

As can be observed in the zero field data set of Figure 4-19 there is random high resistance switching, first assumed to be noise. After completing the experiment and gathering the data, it has become evident that this high resistance switching in the absence of a magnetic field may be due to (Spin Transfer Torque Induced Spin Blockade). The 10nA filtered spins act on the particle through STT reducing the spin energies of the system to the point where it was no longer favorable to release electrons for continued current flow through spin blockade. As the system no longer permitted current flow, thermal energies began to act on the precessions again making them energetically favorable for electron transport. This STTISB concept may have validity as evident by the applied field, as it begins to become the dominant acting force overshadowing the STTISB in the more stable high resistive mode. If this is truly the acting mechanism, then we have managed to accomplish something quite fascinating, the energy required for the quantum mechanical switching of spin states is orders of magnitude smaller than the equivalent energy in conventional systems.

It is noteworthy that this experiment has for the first time explicitly demonstrated the quantum-mechanical nature of this device. Indeed, the following important observations should be highlighted. First, the possible values of the resistance are not continuous, like in conventional devices, but discrete, as expected according to the quantum physics. Second, the transition between these states is probabilistic, the transition probability depends on the applied magnetic field. Indeed, according to the quantum mechanics, each state is defined by a certain wave function, which in turn defines the probability of this state. Therefore, it is within reason that the probability of these magnetic states strongly depend on the magnetic field applied. Third, an extremely high

magnetoresistance value, on the order of 10^6 could be observed, clearly indicating extreme spin filtering behavior. This is remarkable because such high values of the magnetoresistance are comparable to those in CMOS technologies and therefore these devices have the potential to break into the competitive trillion-dollar multi-segment information processing market in the near future.

4.5. **Summary**

Although there is no widely accepted theory to understand the behavior of spintronic devices in the sub-10nm range we have built upon a hypothesis which was previously simulated and then tested through rigorous micro & nano fabrication resulting in experimental data that closely fits the proposed theoretical curve. We designed, fabricated and tested three separate Spin Transfer Torque Magnetic Tunneling devices.

One device the 3D tri-layer STT-MTJ utilized the principles of a standard STT-MTJ such as that reported in section 4.3.3 “FIB-MTJ” listed in table 3 below with the added tunneling oxide and ferromagnetic film. We were able to demonstrate a single addressed device with three discreet states corresponding to sequential switching of the spin orientation of each ferromagnetic layer in the device. This architecture seems an ideal contribution to applications in neuromorphic computation.

The second device “particle MTJ” also modified the “FIB-MTJ” device reported above with the addition of using ferromagnetic nanoparticles embedded in the tunneling oxide layer. The sub-4nm particles were used as a method of overcoming the minimum feature limitations of micro and nano fabrication to investigate magnetoresistance (MR) in smaller quantum-mechanical devices. We were able to achieve an MR of 120%, twice that of the 60% MR from the FIB-MTJ and four times greater than the 30% reported in the

AFM tip experiment. Here we have contributed to the successful demonstration of a novel nanoparticle based architecture in a STT-MTJ device with increased MR.

Table 3: Pros and Cons of each device

	Version 1 STM probe	Version 2 FIB MTJ	Version 3 Particle MTJ	Version 4 Nanopore MTJ
Advantages	Exploit small size of AFM tip	Nanoscale devices were achieved with FIB overcoming photolithography limitations	Bottom up approach achieve small devices via nanoparticles embedded in structure removes the need for small feature lithography	Bottom up architecture exploits anodic disk pore size, mitigating particle aggregation, mass production, **reduce process development timeline**, avoids use of FIB and challenges associated with it
Disadvantages	Mechanical stress; Difficult to FIB; Low throughput	Ion implantation may impact physics of device; Re-deposition from milling; Low throughput	Particle aggregation; FIB is used to reduce aggregation and potential shorts from impact of topography due to particles	Addressing devices via E-beam Lithography

Building off the success of the "particle-MTJ" we devised a novel fabrication architecture that overcame the primary low throughput disadvantage of the previous experiments (table 3). Using nanoporous alumina as a scaffolding we were able to build essentially an assay that permitted mass fabrication of multi-layered, single point particle based MTJs. Instead of taking months to fabricate one device we were able to fabricate millions within the same time on one chip. This contribution permits quick mechanical probing of electric or magnetic analysis of not only quantum mechanical behavior but any behavior on the thin film, nano-particle or single point (quantum dot) regime. Zero lithographic need coupled with varying deposition thicknesses or particle sizes permits quick evaluation of trends based on designed or random variances. While scanning we came across a couple spots which yielded an unprecedented 50,000% MR.

The last time a discovery was made that increased the percent magnetoresistance by a single order of magnitude; it fueled a multibillion dollar hard drive industry for

decades. Here we are reporting 2 orders of magnitude greater than that technology. Should we be correct and the final results presented here be quantum mechanical in nature as hypothesized above and as the experimental results suggest then we have contributed significantly to the probability of room temperature quantum computing in the near future. To further underscore the significance of this achievement, to make spintronic devices competitive, their "On/Off ratio" should be made compatible to that in CMOS technology. Hence, the demonstration of such a high "On/Off" ratio is a groundbreaking experiment with the great potential to make the unprecedented capabilities of spintronics a reality.

5. FUTURE WORKS

It is critical to pursue more novel device fabrication techniques to continue exploring this promising size regime. It would be prudent that future research in this field include cryogenic magnetotransport studies to understand temperature related phenomenon. While highly ordered large scale fabrication techniques in the sub-10nm range is still unrealized, an argument has been made here that suggests continuing studies to prove the insurmountable possibilities that spintronics has to offer in the sub-10nm size regime is worthy. Below are additional works to be completed.

We have also begun to build an addressable array using Electron Beam Lithography techniques as described in section 3 in order to reduce the size of the cross section (area of the MTJ) between two perpendicular streets. Figure 5-1 illustrates the typical architecture of the addressable array. One can see the MTJ stack between the perpendicular streets.

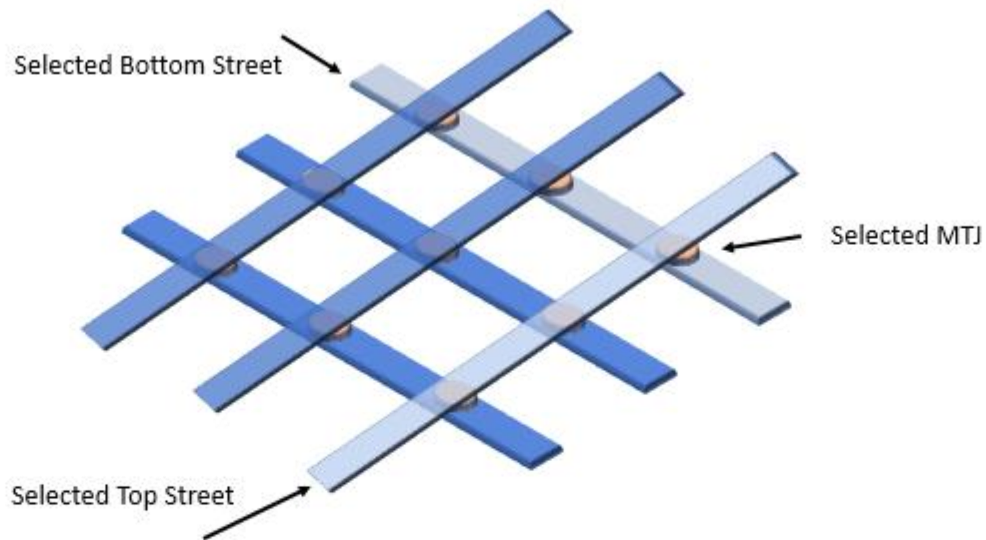

Figure 5-1: Addressable MTJ array architecture

Thus far we have been able to write 100nm lines (bottom streets of the array) between photolithographed electrodes as seen in the Scanning Electron Micrograph (SEM) images in Figure 5-2 while Figure 5-3 is a high resolution SEM of the 100nm diameter wires with approximately 100nm pitch.

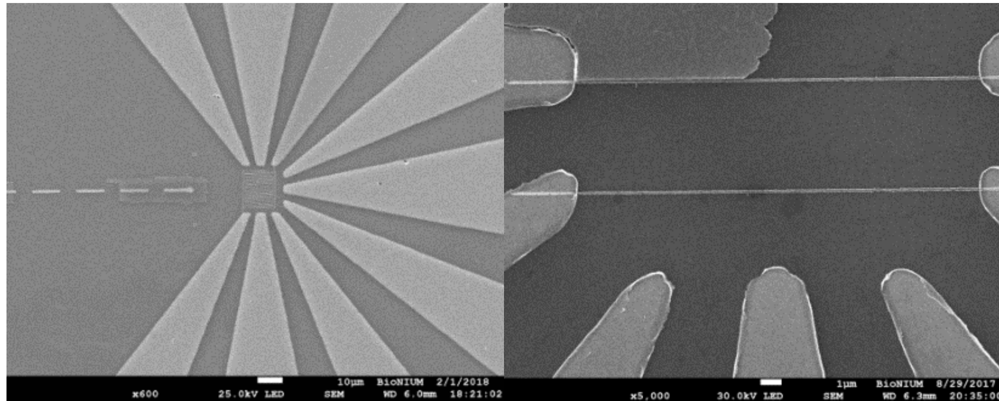

Figure 5-2: SEM images of photolithographed electrodes with 100nm Au lines between electrodes lithographed using EBL

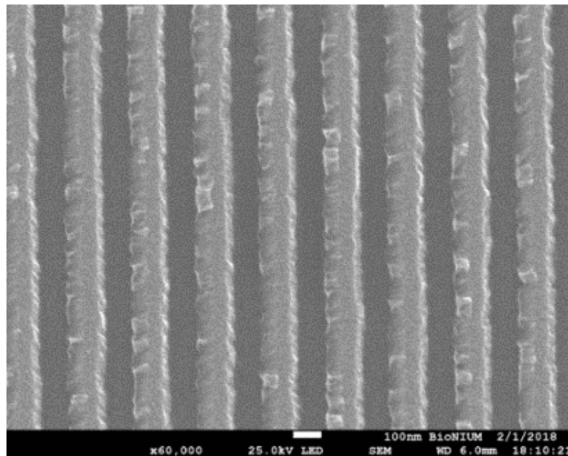

Figure 5-3: SEM images of 100nm Au lines using EBL

Additionally given the success of our latest experiments with porous alumina we can apply the anodic disk architecture using highly ordered nanoporous alumina. Highly ordered nanoporous alumina is costly and could not be justified at the time however, again given the previous results, its use in fabricating devices could be quite successful. Doing so would permit addressable lines (similar to figure 5-1) on both sides of the alumina permitting a full large density memory logic chip.

REFERENCES

[1] J. Fabian, A. Matos-Abiague, C. Ertler, P. Stano, and I. Žutić, “Semiconductor spintronics,” *Acta Phys. Slovaca. Rev. Tutorials*, vol. 57, no. 4–5, pp. 565–907, Aug. 2007.

[2] G. E. Moore, “Cramming More Components Onto Integrated Circuits,” *Proc. IEEE*, vol. 86, no. 1, pp. 82–85, Jan. 1998.

[3] J. M. Shalf and R. Leland, “Computing beyond Moore’s Law,” *Computer (Long. Beach. Calif).*, vol. 48, no. 12, pp. 14–23, Dec. 2015.

[4] Jongyeon Kim, A. Paul, P. A. Crowell, S. J. Koester, S. S. Sapatnekar, Jian-Ping Wang, and C. H. Kim, “Spin-Based Computing: Device Concepts, Current Status, and a Case Study on a High-Performance Microprocessor,” *Proc. IEEE*, vol. 103, no. 1, pp. 106–130, Jan. 2015.

[5] S.-H. Lo, D. A. Buchanan, Y. Taur, and W. Wang, “Quantum-mechanical modeling of electron tunneling current from the inversion layer of ultra-thin-oxide nMOSFET’s,” *IEEE Electron Device Lett.*, vol. 18, no. 5, pp. 209–211, May 1997.

[6] G. Binasch, P. Grünberg, F. Saurenbach, and W. Zinn, “Enhanced magnetoresistance in layered magnetic structures with antiferromagnetic interlayer exchange,” *Phys. Rev. B*, vol. 39, no. 7, pp. 4828–4830, Mar. 1989.

[7] M. N. Baibich, J. M. Broto, A. Fert, F. N. Van Dau, F. Petroff, P. Etienne, G. Creuzet, A. Friederich, and J. Chazelas, “Giant Magnetoresistance of (001)Fe/(001)Cr Magnetic Superlattices,” *Phys. Rev. Lett.*, vol. 61, no. 21, pp. 2472–2475, Nov. 1988.

[8] L. Chang, M. Wang, L. Liu, S. Luo, and P. Xiao, “A brief introduction to giant magnetoresistance,” *Res. Gate*, Dec. 2014.

[9] E. F. Okosodo, J. O. Orimaye, and F. O. Obasogie, “Food and Feeding Ecology of Common Bulbul (Pycnonotus barbatus) in Leventis Foundation Agricultural School Ilesa South Western Nigeria,” *Greener J. Agric. Sci.*, vol. 6, no. 1, pp. 010–016, Jan. 2016.

[10] W. J. Gallagher and S. S. P. Parkin, “Development of the magnetic tunnel junction MRAM at IBM: From first junctions to a 16-Mb MRAM demonstrator chip,” *IBM J. Res. Dev.*, vol. 50, no. 1, pp. 5–23, Jan. 2006.

[11] S. Tehrani, J. M. Slaughter, M. Deherrera, B. N. Engel, N. D. Rizzo, J. Salter, M. Durlam, R. W. Dave, J. Janesky, B. Butcher, K. Smith, and G. Grynkewich, “Magnetoresistive random access memory using magnetic tunnel junctions,” *Proc. IEEE*, vol. 91, no. 5, pp. 703–714, May 2003.

[12] J. M. Slaughter, R. W. Dave, M. DeHerrera, M. Durlam, B. N. Engel, J. Janesky, N. D. Rizzo, and S. Tehrani, "Fundamentals of MRAM technology," *J. Supercond.*, vol. 15, no. 1, pp. 19–25, 2002.

[13] M. Julliere, "Tunneling between ferromagnetic films," *Phys. Lett. A*, vol. 54, no. 3, pp. 225–226, Sep. 1975.

[14] Y. Qi, D. Y. Xing, and J. Dong, "Relation between Julliere and Slonczewski models of tunneling magnetoresistance," *Phys. Rev. B*, vol. 58, no. 5, pp. 2783–2787, Aug. 1998.

[15] S. Ikeda, J. Hayakawa, Y. Ashizawa, Y. M. Lee, K. Miura, H. Hasegawa, M. Tsunoda, F. Matsukura, and H. Ohno, "Tunnel magnetoresistance of 604% at 300K by suppression of Ta diffusion in CoFeB/MgO/CoFeB pseudo-spin-valves annealed at high temperature," *Appl. Phys. Lett.*, vol. 93, no. 8, p. 082508, Aug. 2008.

[16] Freescale-Semiconductors, "Freescale leads industry in commercializing MRAM technology 4 Mbit MRAM memory product now in volume production," *Press release*, 2006.

[17] Everspin Technologies, "Everspin Technologies takes MRAM to higher densities with 16 megabit product introduction," *Press release*, 2010.

[18] Jian-Gang Zhu, "Magnetoresistive Random Access Memory: The Path to Competitiveness and Scalability," *Proc. IEEE*, vol. 96, no. 11, pp. 1786–1798, Nov. 2008.

[19] A. Hatfield, "Everspin debuts first Spin-Torque MRAM for high performance storage systems," 2012.

[20] Toshiba, "Toshiba's new STT-MRAM memory element promises world's best power consumption and to outperform SRAM," 2012.

[21] MRAM-Info, "TDK to present a 8-Mbit STT-MRAM prototype, plans to commercialize the technology in 3-5 years," 2014.

[22] L. Liu, C. F. Pai, D. C. Ralph, and R. A. Buhrman, "Magnetic oscillations driven by the spin hall effect in 3-terminal magnetic tunnel junction devices," *Phys. Rev. Lett.*, vol. 109, no. 18, p. 186602(5), Oct. 2012.

[23] I. M. Miron, K. Garello, G. Gaudin, P. J. Zermatten, M. V. Costache, S. Auffret, S. Bandiera, B. Rodmacq, A. Schuhl, and P. Gambardella, "Perpendicular switching of a single ferromagnetic layer induced by in-plane current injection," *Nature*, vol. 476, no. 7359. pp. 189–193, 11-Aug-2011.

[24] L. Liu, T. Moriyama, D. C. Ralph, and R. A. Buhrman, "Spin-torque ferromagnetic resonance induced by the spin Hall effect," *Phys. Rev. Lett.*, vol. 106, no. 3, p. 036601, Jan. 2011.

[25] A. Hoffmann, "Spin hall effects in metals," *IEEE Trans. Magn.*, vol. 49, no. 10, pp. 5172–5193, Oct. 2013.

[26] L. Liu, O. J. Lee, T. J. Gudmundsen, D. C. Ralph, and R. A. Buhrman, "Current-induced switching of perpendicularly magnetized magnetic layers using spin torque from the spin hall effect," *Phys. Rev. Lett.*, vol. 109, no. 9, p. 096602, Aug. 2012.

[27] Y. Tserkovnyak, A. Brataas, and G. E. W. Bauer, "Enhanced Gilbert Damping in Thin Ferromagnetic Films," *Phys. Rev. Lett.*, vol. 88, no. 11, p. 4, Feb. 2002.

[28] Y. Tserkovnyak, A. Brataas, G. E. W. Bauer, and B. I. Halperin, "Nonlocal magnetization dynamics in ferromagnetic heterostructures," *Rev. Mod. Phys.*, vol. 77, no. 4, pp. 1375–1421, Dec. 2005.

[29] V. V. Naletov, V. Charbois, O. Klein, and C. Fermon, "Quantitative measurement of the ferromagnetic resonance signal by force detection," *Appl. Phys. Lett.*, vol. 83, no. 15, pp. 3132–3134, Oct. 2003.

[30] S. Takahashi and S. Maekawa, "Spin hall effect," in *Spin Current*, vol. 83, no. 9, American Physical Society, 2017, pp. 208–225.

[31] R. L. Stamps, S. Breitkreutz, J. Åkerman, A. V Chumak, Y. Otani, G. E. W. Bauer, J. U. Thiele, M. Bowen, S. A. Majetich, M. Kläui, I. L. Prejbeanu, B. Dieny, N. M. Dempsey, and B. Hillebrands, "The 2014 Magnetism Roadmap," *Journal of Physics D: Applied Physics*, vol. 47, no. 33. IOP Publishing, pp. 1–28, 20-Aug-2014.

[32] A. Hirohata and K. Takanashi, "Future perspectives for spintronic devices," *J. Phys. D. Appl. Phys.*, vol. 47, no. 19, p. 193001, May 2014.

[33] S. Mizukami, Y. Ando, and T. Miyazaki, "Ferromagnetic resonance linewidth for NM/80NiFe/NM films (NM = Cu, Ta, Pd and Pt)," *J. Magn. Magn. Mater.*, vol. 226–230, no. PART II, pp. 1640–1642, Feb. 2001.

[34] S. Ingvarsson, L. Ritchie, X. Y. Liu, G. Xiao, J. C. Slonczewski, P. L. Trouilloud, and R. H. Koch, "Role of electron scattering in the magnetization relaxation of thin (formula presented) films," *Phys. Rev. B - Condens. Matter Mater. Phys.*, vol. 66, no. 21, pp. 1–5, Dec. 2002.

[35] J. C. Rojas-Sánchez, N. Reyren, P. Laczkowski, W. Savero, J. P. Attané, C. Deranlot, M. Jamet, J. M. George, L. Vila, and H. Jaffrès, "Spin pumping and inverse spin hall effect in platinum: The essential role of spin-memory loss at metallic interfaces," *Phys. Rev. Lett.*, vol. 112, no. 10, p. 106602, Mar. 2014.

[36] E. E. Fullerton, D. Stoeffler, K. Ounadjela, B. Heinrich, Z. Celinski, and J. A. C. Bland, "Structure and magnetism of epitaxially strained Pd(001) films on Fe(001): Experiment and theory," *Phys. Rev. B*, vol. 51, no. 10, pp. 6364–6378, Mar. 1995.

[37] Y. Sun, H. Chang, M. Kabatek, Y. Y. Song, Z. Wang, M. Jantz, W. Schneider, M. Wu, E. Montoya, B. Kardasz, B. Heinrich, S. G. E. Te Velthuis, H. Schultheiss, and A. Hoffmann, "Damping in yttrium iron garnet nanoscale films capped by platinum," *Phys. Rev. Lett.*, vol. 111, no. 10, p. 106601, Sep. 2013.

[38] W. L. Lim, N. Ebrahim-Zadeh, J. C. Owens, H. G. E. Hentschel, and S. Urazhdin, "Temperature-dependent proximity magnetism in Pt," *Appl. Phys. Lett.*, vol. 102, no. 16, p. 162404, Apr. 2013.

[39] F. Wilhelm, P. Poulopoulos, G. Ceballos, H. Wende, K. Baberschke, P. Srivastava, D. Benea, H. Ebert, M. Angelakeris, N. K. Flevaris, D. Niarchos, A. Rogalev, and N. B. Brookes, "Layer-resolved magnetic moments in Ni/Pt multilayers," *Phys. Rev. Lett.*, vol. 85, no. 2, pp. 413–416, Jul. 2000.

[40] S. A. Adelman and J. D. Doll, "Generalized Langevin equation approach for atom/solid-surface scattering: Collinear atom/harmonic chain model," *J. Chem. Phys.*, vol. 61, no. 10, pp. 4242–4245, Nov. 1974.

[41] N. A. Spaldin, *Magnetic Materials: Fundamentals and Applications*, 2nd Editio. Cambridge University Press, 2011.

[42] B. D. Cullity and C. D. Graham, *Introduction to Magnetic Materials*. Wiley-IEEE Press, 2009.

[43] J. M. D. Coey, *Magnetism and Magnetic Materials*, 1st Editio. Cambridge University Press, 2010.

[44] B. D. Cullity and C. D. Graham, *Introduction to Magnetic Materials*. Wiley-IEEE Press, 2009.

[45] J. M. D. Coey, *Magnetism and Magnetic Materials*, 1st Editio. Cambridge University Press, 2010.

[46] W. Heisenberg, "On the theory of ferromagnetism," *Z. Phys.*, vol. 49, pp. 619–636, 1928.

[47] H. Pender and R. L. Jones, "The Annealing of Steel in an Alternating Magnetic Field," *Phys. Rev.*, vol. 1, no. 4, pp. 211–214, 1913.

[48] A. I. Schindler, R. H. Kernohan, and J. Weertman, "Effect of Irradiation on Magnetic Properties of Fe-Ni Alloys," *J. Appl. Phys.*, vol. 35, no. 9, pp. 2640–2646, Sep. 1964.

[49] R. D. Brown, J. R. Cost, and J. T. Stanley, "Effects of neutron irradiation on magnetic permeability of amorphous and crystalline magnetic alloys," *J. Appl. Phys.*, vol. 55, no. 6, pp. 1754–1756, Mar. 1984.

[50] C. P. Bean and J. D. Livingston, "Superparamagnetism," *J. Appl. Phys.*, vol. 30, no. 4, pp. S120–S129, Apr. 1959.

[51] Y. Gossuin, P. Gillis, A. Hocq, Q. L. Vuong, and A. Roch, "Magnetic resonance relaxation properties of superparamagnetic particles," *Wiley Interdiscip. Rev. Nanomedicine Nanobiotechnology*, vol. 1, no. 3, pp. 299–310, May 2009.

[52] E. Tahmasebi and Y. Yamini, "Facile synthesis of new nano sorbent for magnetic solid-phase extraction by self assembling of bis-(2,4,4-trimethyl pentyl)-dithiophosphinic acid on Fe3O4@Ag core@shell nanoparticles: Characterization and application," *Anal. Chim. Acta*, vol. 756, pp. 13–22, Dec. 2012.

[53] M. F. Collins and J. B. Forsyth, "The magnetic moment distribution in some transition metal alloys," *Philos. Mag.*, vol. 8, no. 87, pp. 401–410, Mar. 1963.

[54] D. I. Bardos, "Mean Magnetic Moments in bcc Fe–Co Alloys," *J. Appl. Phys.*, vol. 40, no. 3, pp. 1371–1372, Mar. 1969.

[55] R. H. Victora and L. M. Falicov, "Calculated magnetization of iron-cobalt disordered alloys," *Phys. Rev. B*, vol. 30, no. 1, pp. 259–262, Jul. 1984.

[56] M. J. Madou, *Fundamentals of Microfabrication: The Science of Miniaturization*, 2nd Editio. CRC Press, 2002.

[57] S. Wolf and R. N. Tauber, *Silicon Processing for the VLSI Era, Volume 1: Process Technology*, 2nd Editio. Lattice Press, 1999.

[58] V. Bhatt, S. Chandra, and C. Singh, "Microstructures using RF sputtered PSG film as a sacrificial layer in surface micromachining," *Sadhana*, vol. 34, no. 4, pp. 557–562, Aug. 2009.

[59] D. B. Hall, P. Underhill, and J. M. Torkelson, "Spin coating of thin and ultrathin polymer films," *Polym. Eng. Sci.*, vol. 38, no. 12, pp. 2039–2045, Dec. 1998.

[60] R. A. Pethrick and K. E. Rankin, "Criteria for uniform thin film formation for polymeric materials," *J. Mater. Sci. Mater. Electron.*, vol. 10, pp. 141–144, 1999.

[61] T. A. Brunner, "Optimization of optical properties of resist processes," in *Advances in Resist Technology and Processing VIII*, 1991, pp. 297–308.

[62] A. Many, Y. Goldstein, and N. B. Grover, *Semiconductor Surfaces*. North-Holland, 1965.

[63] L. M. Ephrath, “Reactive Ion Etching,” US4283249A, 1981.

[64] J. Baran, A. Duda, A. Kowalski, R. Szymanski, and S. Penczek, “Intermolecular chain transfer to polymer with chain scission: general treatment and determination of kp/ktr in L,L-lactide polymerization,” *Macromol. Rapid Commun.*, vol. 18, no. 4, pp. 325–333, Apr. 1997.

[65] J. M. Havard, N. Vladimirov, J. M. J. Fréchet, S. Yamada, C. G. Willson, and J. D. Byers, “Photoresists with Reduced Environmental Impact: Water-Soluble Resists Based on Photo-Cross-Linking of a Sugar-Containing Polymethacrylate,” *Macromolecules*, vol. 32, no. 1, pp. 86–94, Jan. 1999.

[66] H. Klose, R. Sigush, and W. Arden, “Image reversal of positive photoresist: Characterization and modeling,” *IEEE Trans. Electron Devices*, vol. 32, no. 9, pp. 1654–1661, Sep. 1985.

[67] W. E. Feely, J. C. Imhof, and C. M. Stein, “The role of the latent image in a new dual image, aqueous developable, thermally stable photoresist,” *Polym. Eng. Sci.*, vol. 26, no. 16, pp. 1101–1104, Sep. 1986.

[68] M. Spak, D. Mammato, S. Jain, and D. Durham, “Mechanism and lithographic evaluation of image reversal in AZ 5214 photoresist,” in *Seventh International Technical Conference on Photopolymers*, 1985.

[69] C. Schneider, J. Smyth, and A. Watts, “Automated photolithography critical dimension controls in a complex, mixed technology, manufacturing fab,” in *2001 IEEE/SEMI Advanced Semiconductor Manufacturing Conference (IEEE Cat. No.01CH37160)*, pp. 33–40.

[70] A. E. Grigorescu and C. W. Hagen, “Resists for sub-20-nm electron beam lithography with a focus on HSQ: state of the art,” *Nanotechnology*, vol. 20, no. 29, p. 292001, Jul. 2009.

[71] E. Kratschmer, “An electron-beam microcolumn with improved resolution, beam current, and stability,” *J. Vac. Sci. Technol. B Microelectron. Nanom. Struct.*, vol. 13, no. 6, p. 2498, Nov. 1995.

[72] V. R. Manfrinato, L. Zhang, D. Su, H. Duan, R. G. Hobbs, E. A. Stach, and K. K. Berggren, “Resolution Limits of Electron-Beam Lithography toward the Atomic Scale,” *Nano Lett.*, vol. 13, no. 4, pp. 1555–1558, Apr. 2013.

[73] R. F. Egerton, P. Li, and M. Malac, “Radiation damage in the TEM and SEM,” *Micron*, vol. 35, no. 6, pp. 399–409, Aug. 2004.

[74] Z. Wang, J. E. Alaniz, W. Jang, J. E. Garay, and C. Dames, “Thermal Conductivity of Nanocrystalline Silicon: Importance of Grain Size and Frequency-Dependent Mean Free Paths,” *Nano Lett.*, vol. 11, no. 6, pp. 2206–2213, Jun. 2011.

[75] A. A. Talin, K. A. Dean, and J. E. Jaskie, “Field emission displays: a critical review,” *Solid. State. Electron.*, vol. 45, no. 6, pp. 963–976, Jun. 2001.

[76] R. Buhl, E. Moll, and H. Daxinger, “Method and apparatus for evaporating material under vacuum using both an arc discharge and electron beam,” US4448802A, 1981.

[77] J. A. Thornton, “The microstructure of sputter-deposited coatings,” *J. Vac. Sci. Technol. A Vacuum, Surfaces, Film.*, vol. 4, no. 6, pp. 3059–3065, Nov. 1986.

[78] S. M. Rossnagel and J. Hopwood, “Magnetron sputter deposition with high levels of metal ionization,” *Appl. Phys. Lett.*, vol. 63, no. 24, pp. 3285–3287, Dec. 1993.

[79] M. Albertine and A.-M. Van Wijck, “Atomic layer deposition,” US6585823B1, 2000.

[80] I.-S. Jeon, S.-B. Kang, H.-S. Lim, and G. Choi, “Method of manufacturing a barrier metal layer using atomic layer deposition,” US6399491B2, 2002.

[81] H.-K. Lee, H.-Y. Lee, and J.-M. Jeon, “Codeposition of micro- and nano-sized SiC particles in the nickel matrix composite coatings obtained by electroplating,” *Surf. Coatings Technol.*, vol. 201, no. 8, pp. 4711–4717, Jan. 2007.

[82] M. Tatchell-Evans, N. Kapur, J. Summers, H. Thompson, and D. Oldham, “An experimental and theoretical investigation of the extent of bypass air within data centres employing aisle containment, and its impact on power consumption,” *Appl. Energy*, vol. 186, pp. 457–469, Jan. 2017.

[83] R. Landauer, “Irreversibility and Heat Generation in the Computing Process,” *IBM J. Res. Dev.*, vol. 5, no. 3, pp. 183–191, Jul. 1961.

[84] A. Pushp, T. Phung, C. Rettner, B. P. Hughes, S.-H. Yang, and S. S. P. Parkin, “Giant thermal spin-torque–assisted magnetic tunnel junction switching,” *Proc. Natl. Acad. Sci.*, vol. 112, no. 21, pp. 6585–6590, May 2015.

[85] G. A. Prinz, “Magnetoelectronics,” *Science (80-.).*, vol. 282, no. 5394, pp. 1660–1663, Nov. 1998.

[86] G. M. Müller, J. Walowski, M. Djordjevic, G.-X. Miao, A. Gupta, A. V. Ramos, K. Gehrke, V. Moshnyaga, K. Samwer, J. Schmalhorst, A. Thomas, A. Hütten, G. Reiss, J. S. Moodera, and M. Münzenberg, “Spin polarization in half-metals probed by femtosecond spin excitation,” *Nat. Mater.*, vol. 8, no. 1, pp. 56–61, Jan. 2009.

[87] D. C. Ralph and M. D. Stiles, “Spin transfer torques,” *J. Magn. Magn. Mater.*, vol. 320, no. 7, pp. 1190–1216, Apr. 2008.

[88] M. Gajek, J. J. Nowak, J. Z. Sun, P. L. Trouilloud, E. J. O'Sullivan, D. W. Abraham, M. C. Gaidis, G. Hu, S. Brown, Y. Zhu, R. P. Robertazzi, W. J. Gallagher, and D. C. Worledge, "Spin torque switching of 20 nm magnetic tunnel junctions with perpendicular anisotropy," *Appl. Phys. Lett.*, vol. 100, no. 13, p. 132408, Mar. 2012.

[89] Y. Huai, H. Gan, Z. Wang, P. Xu, X. Hao, B. K. Yen, R. Malmhall, N. Pakala, C. Wang, J. Zhang, Y. Zhou, D. Jung, K. Satoh, R. Wang, L. Xue, and M. Pakala, "High performance perpendicular magnetic tunnel junction with Co/Ir interfacial anisotropy for embedded and standalone STT-MRAM applications," *Appl. Phys. Lett.*, vol. 112, no. 9, p. 092402, Feb. 2018.

[90] C. Melcher and M. Ptashnyk, "Landau--Lifshitz--Slonczewski Equations: Global Weak and Classical Solutions," *SIAM J. Math. Anal.*, vol. 45, no. 1, pp. 407–429, Jan. 2013.

[91] T. L. Gilbert, "Classics in Magnetics A Phenomenological Theory of Damping in Ferromagnetic Materials," *IEEE Trans. Magn.*, vol. 40, no. 6, pp. 3443–3449, Nov. 2004.

[92] L. Abelmann, S. K. Khizroev, D. Litvinov, J.-G. Zhu, J. A. Bain, M. H. Kryder, K. Ramstöck, and C. Lodder, "Micromagnetic simulation of an ultrasmall single-pole perpendicular write head," *J. Appl. Phys.*, vol. 87, no. 9, pp. 6636–6638, May 2000.

[93] V. L. Safonov, *Nonequilibrium Magnons*. Wiley-VCH, 2012.

[94] J. Hong, P. Liang, V. L. Safonov, and S. Khizroev, "Energy-efficient spin-transfer torque magnetization reversal in sub-10-nm magnetic tunneling junction point contacts," *J. Nanoparticle Res.*, vol. 15, no. 4, p. 1599, Apr. 2013.

[95] J. Hong, P. Liang, V. L. Safonov, and S. Khizroev, "Energy-efficient spin-transfer torque magnetization reversal in sub-10-nm magnetic tunneling junction point contacts," *J. Nanoparticle Res.*, vol. 15, no. 4, p. 1599, Apr. 2013.

[96] R. P. Andres, T. Bein, M. Dorogi, S. Feng, J. I. Henderson, C. P. Kubiak, W. Mahoney, R. G. Osifchin, and R. Reifenberger, "'Coulomb Staircase' at Room Temperature in a Self-Assembled Molecular Nanostructure," *Science (80-.).*, vol. 272, no. 5266, pp. 1323–1325, May 1996.

[97] J. Hong, B. Lambson, S. Dhuey, and J. Bokor, "Experimental test of Landauer's principle in single-bit operations on nanomagnetic memory bits," *Sci. Adv.*, vol. 2, no. 3, p. e1501492, Mar. 2016.

[98] H. Sato, S. Ikeda, and H. Ohno, "Magnetic tunnel junctions with perpendicular easy axis at junction diameter of less than 20nm," *Japanese Journal of Applied Physics*, vol. 56, no. 8. IOP Publishing, p. 0802A6(9), Aug-2017.

[99] J. Hong, A. Hadjikhani, M. Stone, F. I. Allen, V. Safonov, P. Liang, J. Bokor, and S. Khizroev, "The Physics of Spin-Transfer Torque Switching in Magnetic Tunneling Junctions in Sub-10 nm Size Range," *IEEE Trans. Magn.*, vol. 52, no. 7, pp. 1–4, Jul. 2016.

[100] H. Sato, E. C. I. Enobio, M. Yamanouchi, S. Ikeda, S. Fukami, S. Kanai, F. Matsukura, and H. Ohno, "Properties of magnetic tunnel junctions with a MgO/CoFeB/Ta/CoFeB/MgO recording structure down to junction diameter of 11 nm," *Appl. Phys. Lett.*, vol. 105, no. 6, p. 062403, Aug. 2014.

[101] S. Aravamudhan, K. Luongo, P. Poddar, H. Srikanth, and S. Bhansali, "Porous silicon templates for electrodeposition of nanostructures," *Appl. Phys. A Mater. Sci. Process.*, vol. 87, no. 4, pp. 773–780, Apr. 2007.

VITA

KEVIN LUONGO

2016-Present	Nanofabrication Facility Manager University of Miami Miami, Florida
2010-2018	Doctoral Candidate, Electrical Engineering Florida International University Miami, Florida
2012-2016	Senior Equipment Engineer Florida International University Miami, Florida
2009-2012	Draper Lab Fellow Draper National Labs Tampa, Florida
2002-2009	Research Engineer University of South Florida Tampa, Florida
2002-2008	M.S., Electrical Engineering University of South Florida Tampa, Florida
2006-2007	Research Engineer Sandia National Laboratory Livermore, California
1999-2001	A.S., Dept. of Engineering Saint Petersburg College St Pete, Florida

PUBLICATIONS

1. Luongo, K., Stone, M., Pimentel, K., et al. Quantum mechanical logic switching observed at room temperature in mass fabrication of nanoparticle magnetic tunneling junctions using nanoporous alumina. Presently in the works, (2018)
2. Hong, J., Stone, M., Navarrete, B., Luongo, K., Zheng, Q., Yuan, Z., Xia, K., Xu, N., Bokor, J., You, L., Khizroev, S., 3D multilevel spin transfer torque devices. Appl. Phys. Lett. 112, 112402 (2018).

3. Navarrete, B., Stone, M., Luongo, K., et al. Properties of magnetic tunneling junction devices with characteristic sizes in sub-5-nm range. 2017 Fifth Berkeley Symposium on Energy Efficient Electronic Systems (E3S), 1–3 (IEEE, 2017).
4. Stone, M., Hong, J., Hadjikhani, A., Guduru, R., Manoussakis, A., Stimphil, E., Luongo, K., Liang, P., Safonov, V., Bokor, J., Khizroev, S., Anomalous properties of sub-10-nm magnetic tunneling junctions. in Energy Efficient Electronic Systems (E3S), 2015 Fourth Berkeley Symposium on 1–3 (IEEE, 2015).
5. Luongo, K. et al. Microfluidic device for trapping and monitoring three dimensional multicell spheroids using electrical impedance spectroscopy. Biomicrofluidics 7(3), 034108 (2013).
6. Khanna, P., Luongo, K., Strom, J. A. & Bhansali, S. Axial and shear fracture strength evaluation of silicon microneedles. Microsyst. Technol. 16, 973–978 (2010).
7. Khanna, P., Luongo, K., Strom, J. A. & Bhansali, S. Sharpening of hollow silicon microneedles to reduce skin penetration force. J. Micromechanics Microengineering 20, 45011 (2010).
8. Aravamudhan, S., Luongo, K., Poddar, P., Srikanth, H. & Bhansali, S. Porous silicon templates for electrodeposition of nanostructures. Appl. Phys. A Mater. Sci. Process. 87, 773–780 (2007).
9. Vasic, R. et al. Dielectric relaxation in nanopillar NiFe–silicon structures in high magnetic fields. Curr. Appl. Phys. 7, 34–38 (2007).
10. Luongo, K., Sine, A. & Bhansali, S. Development of a highly sensitive porous Si-based hydrogen sensor using Pd nano-structures. in Sensors and Actuators, B: Chemical 111–112, 125–129 (2005).
11. Simmons, B. A., Cummings, E. B., Davalos, R. V., Reichmuth, D., Krafcik, K. L., Salmi, J., Vandevreugde, J., Ponce, P., Syed, Y., Luongo, K., Sabounchi, P., Universal Bioprocessor LDRD Final Report. SAND2006-6704 (2006)
12. Hydrogen sensor based on Pd diffused nanoporous silicon; pat.# 7,992,425.
13. Method for the assembly of nanowire interconnects. (2006); pat.# 7,112,525.